Research Square

Preprints are preliminary reports that have not undergone peer review.
They should not be considered conclusive, used to inform clinical practice,
or referenced by the media as validated information.

S100B⁺ Interstitial Cells are Proliferative, Vesicle-Producing, and Pigment- Accumulating Regulators of Morphofunctional Heterogeneity in the Heart's Pacemaker

Rostislav Bychkov

rosti.byshkov@gmail.com

National Institute on Aging

Magdalena Juhaszova

National Institute on Aging

Miguel Calvo-Rubio Barrera

National Institute on Aging

Richard Telljohann

National Institute on Aging

Sophia Beshkov

National Institute on Aging

Lorenzo Donald

National Institute on Aging

Edward Lakatta

National Institute on Aging

Research Article

Keywords: S100B, HCN4-pacemaker, telocytes, amoeboid cells, pigmented vesicles, proliferative nests

Posted Date: November 23rd, 2026

DOI: https://doi.org/10.21203/rs.3.rs-11708894/v1

License: This work is licensed under a Creative Commons Attribution 4.0 International License.
Read Full License

Additional Declarations: No competing interests reported.

S100B^{+} Interstitial Cells are Proliferative, Vesicle-Producing, and Pigment-Accumulating Regulators of Morphofunctional Heterogeneity in the Heart's Pacemaker

Bychkov Rostislav, PhD,[1*] Juhaszova Magdalena, PhD,[1] Calvo-Rubio Barrera Miguel, PhD,[2] Richard Telljohann, MS,[1] Beshkov Sophia,[2] Lorenzo A.H. Donald MS,[1] Edward G. Lakatta, MD,[1*]

1 Laboratory of Cardiovascular Science, Intramural Research Program, National Institute on Aging, National Institute of Health, Baltimore, MD.

2 Translational Gerontology Branch, Intramural Research Program, National Institute on Aging, National Institutes of Health, Baltimore, MD.

***Corresponding authors**

Brief title: Proliferative S100B^{+} cells shape SAN cytoarchitecture

Address for Correspondence:

Dr. Rostislav Bychkov

Laboratory of Cardiovascular Science, NIA/NIH

Biomedical Research Center, 251 Bayview Boulevard, Baltimore, Maryland 21224

E-mail: rostislav.bytchkov@nih.gov

Phone: 410-558-8076

Fax: 410-558-8200

Dr. Edward G. Lakatta

Laboratory of Cardiovascular Science, NIA/NIH

Biomedical Research Center, 251 Bayview Boulevard, Baltimore, Maryland 21224

E-mail: LakattaE@mail.nih.gov

Phone: 410-558-8202

† For editorial communications, proofs, and reprints, please contact Dr. Rostislav Bychkov

From the Laboratory of Cardiovascular Science, Intramural Research Program, National Institute on Aging, National Institutes of Health, Baltimore, Maryland, USA.

This work was supported by the Intramural Research Program of the National Institutes of Health, National Institute on Aging. The authors have reported that they have no relationships or conflicts of interest relevant to the contents of this paper to disclose.

Abstract

The sinoatrial node (SAN) exhibits structural and functional heterogeneity. While $HCN4^+$ pacemaker cells have been characterized, the identity and histological organization of SAN interstitial cells remain poorly defined. To characterize the phenotype, proliferative capacity, cytoarchitecture, and ultrastructure of $S100B^+$ interstitial cells in relation to pacemaker tissue heterogeneity. Confocal imaging of immunolabeled SAN whole mounts and transmission electron microscopy (TEM) were used to characterize $S100B^+$ interstitial cells. Proliferation was assessed by 5-ethynyl-2′-deoxyuridine (EdU) incorporation. $S100B^+$ interstitial cells exhibited three morphotypes: patchy (discrete clusters separated by $S100B^-$ gaps), contiguous (continuous distribution with variable density), and solitary (dispersed individual cells). For the first time, we identified proliferative nests of $S100B^+$ interstitial cells incorporating EdU, indicating active DNA synthesis. Intracellular pigment was localized within vesicular structures resembling melanosomes (200–500 nm in diameter). TEM also revealed pigment-containing vesicles within cells and in the interstitium, consistent with vesicle production and extracellular release. The spatial organization of $S100B^+$ cells suggests a potential proliferation–dispersal mechanism in which cells proliferate within nests and newly generated cells disperse into the surrounding tissue, potentially giving rise to patchy, contiguous and solitary morphotypes from nest-associated populations. $S100B^+$ interstitial cells constitute a proliferative, vesicle-producing, pigment-associated population contributing to SAN cytoarchitecture. Nest-associated expansion and spatial redistribution may generate structural heterogeneity with potential implications for pacemaker function and tissue remodeling. These findings identify $S100B^+$ immunoreactive interstitial cells, distinct from peripheral glial cells, as a previously underrecognized cellular population within the cardiac pacemaker.

Keywords: S100B; HCN4-pacemaker; telocytes; amoeboid cells; pigmented vesicles; proliferative nests.

INTRODUCTION

The three-dimensional $HCN4^+$ meshwork of the sinoatrial node (SAN) provides a morphological framework for the primary cardiac pacemaker (Bychkov et al. 2020). The cellular mechanisms underlying pacemaker automaticity are governed by the coupled-clock system, which integrates sarcolemmal ion channel cycling with rhythmic sarcoplasmic reticulum Ca^{2+} release (Lakatta et al. 2010). However, when pacemaker cells are examined within the structural context of intact tissue, the picture becomes more complex. Although functional SAN heterogeneity has been characterized in terms of regional variations in action potential kinetics, conduction velocity, and autonomic responsiveness, the relationship of this heterogeneity to tissue cytoarchitecture and cellular phenotype remains less well understood. While the molecular identity of SAN pacemaker cells has been mapped at single-cell resolution (Lim et al. 2024), the identity and organizational roles of non-pacemaker populations embedded within the $HCN4^+$-immunoreactive meshwork have received limited systematic investigation.

We identified a previously unrecognized population of S100B-immunoreactive interstitial cells within the SAN, morphologically distinct from peripheral glial cells (Bychkov et al. 2022). The S100 protein family, including S100B, comprises Ca^{2+}-binding proteins involved in physiological processes such as calcium homeostasis, proliferation, migration, differentiation, and inflammation (Donato et al. 2009, 2013). The biological effects of S100 proteins depend on the cellular context, including the phenotype of S100-expressing cells and their spatial organization within tissue. Dysregulation of S100

proteins has been implicated in cardiovascular diseases, cancer, and neurodegenerative disorders (Bresnick et al. 2015; Michetti et al. 2019; Zhou et al. 2023).

Among the S100-family proteins, S100B is of particular interest because of its predominantly neural tissue distribution and its use as a glial marker in histology. It functions intracellularly as a Ca^{2+} sensor and extracellularly as a RAGE-dependent signaling molecule (Michetti et al. 2012; Villarreal et al. 2011). Its effects are concentration-dependent, ranging from neuroprotection and cell survival at nanomolar levels to oxidative stress and cell injury at micromolar levels (Bianchi et al. 2011; Saleh et al. 2013). S100B is particularly relevant to the sinoatrial node (SAN), the heart's primary pacemaker, because both neural tissue and the SAN are excitable tissues, raising the question of whether S100B has similar or distinct roles in these contexts. Characterizing S100B-expressing cell populations and their spatial organization in the SAN may help clarify their relationship to SAN cytoarchitecture and function.

In the heart, S100B has emerged as a marker of the intrinsic cardiac autonomic nervous system (Scherschel et al. 2019). Cardiac glial cells release S100B during interventional procedures such as atrial fibrillation ablation (Scherschel et al. 2019), and extracellular S100B modulates energy metabolism, apoptosis, calcium homeostasis, and excitability (Donato et al. 2009; Michetti et al. 2012). Functionally, S100B suppresses the firing rate of intracardiac neurons (Scherschel et al. 2019), and nanomolar concentrations significantly alter spontaneous pacemaker activity in SAN tissue (Bychkov et al. 2022). Similar modulation of neuronal activity by S100B released by astrocytes has been described in neuronal circuits controlling mastication (Morquette et al. 2015), suggesting a broader role in rhythm regulation across excitable systems.

We previously identified a distinct population of S100B$^+$ interstitial cells embedded within the HCN4$^+$ pacemaker meshwork of the SAN, clearly separable from S100B$^+$/GFAP$^+$ peripheral glial cells associated with SAN nerves (Bychkov et al. 2022). Despite their localization within the pacemaker core, these cells have not been incorporated into prevailing structural models of the SAN, which largely emphasize cardiomyocytes, fibroblasts, vasculature, and neural elements (Anderson et al. 2009). As a result, this S100B$^+$ interstitial population has remained structurally and functionally underrecognized, and its contribution to SAN organization has not been systematically examined.

In the present study, we used high-resolution confocal tiled imaging, immunolabeling, EdU incorporation analysis, and transmission electron microscopy to investigate the distribution, morphology, proliferative activity, and ultrastructure of S100B$^+$ interstitial cells in the murine sinoatrial node (SAN). Our analyses revealed distinct vesicular features and intracellular pigment accumulation in these cells. By characterizing their spatial organization and morphological diversity, we identified S100B$^+$ nests as a distinct cytoarchitectural feature of the SAN. These morphological findings challenge the traditional view of the SAN as a static pacemaker cells meshwork and reveal a previously overlooked interstitial component of pacemaker tissue heterogeneity. Together with our previous study demonstrating that S100B regulates spontaneous spiking activity in SAN pacemaker cells, these findings broaden the characterization of S100B in the SAN by complementing our earlier functional observations with an analysis of SAN morphotypes and their potential relationship to proliferative nests.

METHODS

Animal Model and Tissue Preparation

All experimental procedures were approved by the National Institute on Aging Animal Care and Use Committee and conformed to the *Guide for the Care and Use of Laboratory Animals* (NIH Publication No. 85-23, revised 2011). Male C57BL/6J mice (n = 15; ages 3–6 months) were used for confocal imaging and EdU incorporation studies. Additional mice (n = 5; ages 3–6 months) were used for transmission electron microscopy. Animals were euthanized by isoflurane overdose followed by cervical dislocation. Hearts were rapidly excised and perfused retrogradely via the aorta with ice-cold phosphate-buffered saline (PBS) to remove blood.

EdU Labeling

EdU Labeling and Proliferation Analysis. To identify proliferating cells within the SAN, EdU (5-ethynyl-2′-deoxyuridine; Cat # 900584 Sigma 1mg/ml) was dissolved in DMSO and added to the drinking water. Mice were maintained on EdU-containing water for 21 consecutive days, allowing cumulative labeling of cells undergoing DNA synthesis during the exposure period. At the end of the labeling period, animals were euthanized and SAN whole-mount preparations were dissected. Incorporated EdU was visualized using the Click-iT EdU Alexa Fluor 488 Imaging Kit (Thermo Fisher Scientific) according to the manufacturer's protocol. Tissues were subsequently immunostained for S100B and HCN4, enabling identification and quantification of proliferating $S100B^{+}$ interstitial cells relative to $HCN4^{+}$ pacemaker cells.

Immunofluorescence and Confocal Imaging

SAN tissue was microdissected under a stereomicroscope, fixed in 4% paraformaldehyde for 2 hours at 4°C, and permeabilized in 0.3% Triton X-100 in PBS for 30 minutes. Tissues were blocked in 5% normal goat serum for 1 hour at room temperature and incubated overnight at 4°C with primary antibodies: rabbit anti-HCN4 (1:200; Alomone Labs), mouse anti-S100B (1:400; Abcam), and chicken anti-GFAP (1:500; Abcam). Secondary antibodies conjugated to Alexa Fluor 488, 555, or 647 (1:500; Thermo Fisher Scientific) were applied for 2 hours at room temperature. Nuclei were counterstained with DAPI (1 µg/mL). Whole-mount preparations were mounted in ProLong Gold Antifade Mountant (Thermo Fisher Scientific).

High-resolution confocal imaging was performed using a Zeiss LSM 980 confocal microscope with 10×, 20×, and 40× objectives. Tiled panoramic reconstructions (up to 5 × 5 mm) were acquired with 10% overlap and stitched using Zen Blue software (Zeiss). Z-stacks were acquired at 1–2 µm intervals to capture the full thickness of the SAN (50–100 µm). Orthogonal sectioning and 3D reconstructions were performed using Zen Blue software.

Transmission Electron Microscopy

SAN tissue was fixed in 2.5% glutaraldehyde and 2% paraformaldehyde in 0.1 M sodium cacodylate buffer (pH 7.4) for 2 hours at room temperature, post-fixed in 1% osmium tetroxide for 1 hour, dehydrated in graded ethanol, and embedded in Epon resin. Semi-thin sections (1 µm) were stained with toluidine blue for light microscopy. Ultrathin sections (70 nm) were stained with uranyl acetate and lead citrate and examined using a

JEOL JEM-1400 transmission electron microscope at 80 kV. Tiled images were acquired and stitched using SerialEM software.

Quantitative Image Analysis

$S100B^+$ cell clusters were defined as aggregations of at least three $S100B^+$-immunoreactive cells that were (i) in direct membrane contact, (ii) connected through intermediate cells of the same type, or (iii) separated from the nearest cluster by a gap or by a region of at least twofold lower local density. Fluorescence intensity profiles along the superior vena cava (SVC) to inferior vena cava (IVC) axis were generated using ImageJ (NIH). Area under the curve (AUC) was calculated using GraphPad Prism 9.

EdU^+ nuclei were counted semi-automatically using the Spots function in Imaris software with a diameter threshold of 5–8 µm and intensity threshold set to 2 standard deviations above background. Manual verification was performed for all automated counts. EdU labeling index was calculated as (EdU^+ nuclei / total $DAPI^+$ nuclei) × 100%.

Statistical Analysis

Data are presented as mean ± standard deviation (SD). One-way ANOVA with Tukey's HSD post hoc test was used for comparisons among three groups. Pairwise comparisons were performed using unpaired Student's *t*-test. Statistical significance was defined as $P < 0.05$. All analyses were performed using GraphPad Prism 9.

RESULTS

Three-Dimensional Architecture and Spatial Morphotypes of $S100B^+$ Interstitial Cells and Regional Pigmentation in the SAN

We previously identified two distinct $S100B^+$ cell populations (Bychkov et al. 2022): (1) $S100B^+/GFAP^+$ peripheral glial cells forming a web with similar 3D cytoarchitecture

194 inside and outside the HCN4$^+$ meshwork, and (2) S100B$^+$/GFAP$^-$ interstitial cells with a
195 non-glial phenotype, intertwined with the HCN4$^+$ pacemaker meshwork (Supplemental
196 **Fig**. 1). The latter population was shown to modulate SAN action potential firing rate and
197 rhythm (Bychkov et al. 2022).

198 Millimeter-scale three-dimensional panoramic reconstructions (Fig. 1)
199 demonstrated that S100B$^+$ interstitial cells are an integral component of the HCN4$^+$
200 pacemaker meshwork but exhibit regional heterogeneity in density and spatial
201 organization. This variability contrasted sharply with the S100B$^+$/GFAP$^+$ peripheral glial
202 web, which maintained a highly regular and conserved reticular architecture across
203 preparations. By comparison, S100B$^+$ interstitial cell clusters varied substantially in size,
204 composition, and spatial arrangement within and between SANs.

205 Clusters were defined as aggregations of at least three S100B$^+$-cells that were (i)
206 in direct membrane contact, (ii) connected through intermediate cells of the same type,
207 or (iii) separated from the nearest cluster by a gap or by a region of at least twofold lower
208 local density. Using these criteria, S100B$^+$ clusters ranged from small groups of three cells
209 to aggregates of ≥50 cells clearly visible in panoramic reconstructions (**Fig.** 1A2, B2).
210 We introduce the term morphotype to define the millimeter-scale macroscopic
211 architecture of the SAN based on the overall spatial distribution of S100B$^+$ interstitial cells.
212 Each SAN whole-mount preparation (n = 17) exhibited a unique distribution pattern.
213 Morphotypes were assigned by comparing these patterns and grouping preparations
214 according to shared features of their macroscopic spatial organization, resulting in three
215 morphotypes: patchy, contiguous, and dispersed.

1. Patchy morphotype: Discrete clusters separated by S100B$^-$ gaps (three representative gaps indicated in **Fig.** 1A2).
2. Contiguous morphotype: Clusters forming a continuous distribution across the meshwork, alternating with lower-density regions but lacking completely empty gaps (**Fig.** 1B2).
3. Solitary morphotype: Individual, non-contiguous S100B$^+$ cells dispersed along the head-to-tail extent of the HCN4$^+$ meshwork without recognizable clusters (**Fig.** 1C2), corresponding to the HCN4-immunoreactive region in **Fig.** 1C1.

Quantitative analysis confirmed that these morphotypes represent distinct organizational states rather than visual impressions. Fluorescence intensity profiles along the SVC–IVC axis from four independent datasets showed significant differences among patchy, contiguous, and solitary morphotypes (**Fig.** 2A; one-way ANOVA: $F(2,57) = 4440.63$, $P < 0.0001$). Tukey's HSD post hoc analysis demonstrated that the patchy morphotype exhibited a modest but significant increase over the solitary morphotype (mean difference = 0.0191, $P = 0.0001$), whereas both were substantially lower than the contiguous morphotype (mean differences = 0.3433 and 0.3242; $P < 0.0001$). Area-under-the-curve (AUC) analysis independently confirmed significant pairwise differences among all three morphotypes ($P < 0.0001$; **Fig.** 2B).

Orthogonal three-dimensional views of the Z-stack dataset (320 µm × 150 µm × 70 µm) enabled simultaneous visualization of XY and XZ planes (**Fig.** 2C), revealing three-dimensional dispersion of S100B$^+$ interstitial cells. Endocardial–epicardial distribution varied regionally: some areas showed uniform distribution (**Fig.** 2C1), whereas others displayed polarization toward the endocardial (**Fig.** 2C2) or epicardial surface (**Fig.** 2C3).

No consistent endo-epicardial pattern correlated with the head, body, or tail of the HCN4$^+$ meshwork.

Transmitted-light imaging demonstrated that S100B$^+$ morphotypes partially overlapped with regional pigmentation patterns (**Fig.** 1). In patchy regions, pigment largely but not completely coincided with S100B$^+$ expression (**Fig.** 1A; yellow circles). In the contiguous morphotype, pigment extended broadly across the HCN4$^+$ meshwork, overlapping yet exceeding S100B$^+$ immunoreactivity (**Fig.** 1B3; red circle). In the solitary morphotype, dispersed S100B$^+$ cells were present but pigment was minimal (**Fig.** 1C3). Thus, pigment distribution and S100B$^+$ immunoreactivity showed coordinated but non-identical spatial organization, indicating partial convergence without complete overlap.

Morphological Diversity, Cluster Organization, and Pigmentation of S100B$^+$ Interstitial Cells

Two main morphological groups of S100B$^+$ interstitial cells were identified within the HCN4$^+$ pacemaker cell meshwork: dendritic and amoeboid cells. Dendritic cells were defined by small somata (approximately 5–10 µm in diameter) and elongated, branching processes extending up to 100 µm, often forming unipolar, bipolar, or multipolar arborizations with spine-like protrusions. Amoeboid cells were characterized by rounded, oval, or irregularly shaped somata and shorter cytoplasmic extensions, generally no longer than the largest somatic diameter. S100B$^+$ cell clusters varied in composition, even within a single preparation: some contained both amoeboid and dendritic phenotypes, whereas others consisted exclusively of one phenotype. The branches of adjacent dendritic S100B$^+$ cells could intertwine, forming irregular local plexuses. **Fig.** 3 compares three clusters containing different numbers of dendritic S100B$^+$ cells. The comparison

illustrates that clusters with fewer dendritic cells have less extensive branch interconnections, whereas clusters with more cells exhibit greater branch intertwining and denser plexus-like arrangements. Clusters dominated by amoeboid $S100B^+$ cells exhibited a progression in cytoarchitecture from scattered single cells or small islets to patchy or contiguous layers as the number of amoeboid cells increased (**Fig.** 4, panels A and B).

In SAN tissue, pigment was readily detectable in transmitted-light images but not in fluorescence images at low magnification (10×, **Fig.** 1). Overlaying transmitted-light images with fluorescence images showing $S100B^+$ and $HCN4^+$ immunoreactivity at higher magnification (40×, Fig. 3 and 4) revealed a spatial correspondence between pigment and $S100B^+$ interstitial cells. The locations and shapes of pigmented cells corresponded to those of $S100B^+$-immunoreactive interstitial cells with dendritic or amoeboid morphologies (**Fig.** 3 and 4). This correspondence was established by overlaying the images and comparing cellular morphology; the pigment itself was not directly labeled. Intracellular pigment distribution varied among cells, even within the same SAN preparation: (1) distributed homogeneously throughout the cell, (2) restricted to the soma, or (3) localized to portions of the soma and/or dendrites.

Hereafter, $S100B^+$ interstitial cells containing intracellular pigment are referred to as $S100B^+$ melanocyte-like interstitial cells. The number of these cells tended to increase with the total number of $S100B^+$ cells within a cluster, so that clusters containing more $S100B^+$ cells generally also contained more $S100B^+$ melanocyte-like interstitial cells (**Fig.** 3A, B and 4A, B). However, this relationship was not absolute. In Figures 3C and 4C, high-density clusters containing more than 20 $S100B^+$ amoeboid or dendritic cells showed

minimal detectable pigment. These observations indicate that S100B expression and pigment production are not obligatorily coupled: an increase in the number of $S100B^+$ cells does not necessarily correspond to an increase in the number of pigment-containing cells.

Intracellular pigment density, reflected by its color ranging from gray or brown to dark black, may influence the detectable signal intensity of S100B fluorescence by absorbing emitted light and attenuating the fluorescence signal. Two dendritic $S100B^+$ interstitial cells in Figure 3, panels A and B (yellow arrows), illustrate this effect. In panel A, dark pigment detected by transmitted light (A4) outlined a bipolar dendritic cell. $S100B^+$ fluorescence colocalized with DAPI in the nucleus, whereas fluorescence in the cytoplasm and dendritic processes was not detectable, potentially because of pigment absorption. In contrast, the cell in panel B contained less pigment, allowing $S100B^+$ fluorescence to be detected throughout the cell.

A similar relationship was observed in amoeboid cells. In Figure 4, Panel A2, only half of the cells visible in transmitted light (Panel A4) were detectable by fluorescence. Therefore, accurate cell counts required overlay of transmitted light and immunofluorescence images. However, dense pigment did not always fully absorb immunofluorescence (**Fig.** 4, Panel B), suggesting variability in pigment type or optical properties. When pigment color was lighter, S100B immunoreactivity and pigment distribution aligned more closely. These observations explain the lack of one-to-one correspondence between confocal fluorescence and transmitted-light images.

Intracellular Coexistence of Pigment-Containing Vesicles and S100B Immunoreactivity

Closer examination of intracellular pigment within S100B$^+$ interstitial cells showed that dense cytoplasmic pigment corresponded to tightly packed pigmented vesicles. When vesicle density decreased and intervesicular spaces became visible, individual vesicles could be distinguished (Fig. 5).

Vesicle detection depended on concentration and optical transparency. In some cells, vesicles were barely detectable (Box 3, Panels 1A and 1B), yet higher-resolution imaging revealed approximately 30 vesicles within the same cell (Panels 3A and 3B). In other cells, hundreds of vesicles occupied a comparable volume and were visible at lower magnification. In these regions, vesicles were so densely packed that individual boundaries could not be resolved, preventing accurate counts (yellow arrows, **Fig.** 5, Panels 1B and 2B). Importantly, S100B$^+$ fluorescence was not fully absorbed by pigment even in areas of high vesicle density, including perinuclear cytoplasm and distal branches (yellow arrows, **Fig.** 5, Panels 2A and 2B). This contrasts with earlier observations (**Fig.** 3 and 4), where densely pigmented vesicles formed a continuous intracellular milieu that obscured S100B$^+$ signal.

Figure 5 shows a cluster of intertwined amoeboid and dendritic, pigmented, vesicle-containing S100B$^+$ interstitial cells embedded within the HCN4$^+$ pacemaker meshwork. These cells formed multiple contact points with adjacent HCN4$^+$ pacemaker cells (**Fig.** 5, Panel 2A), positioning vesicle-rich processes at sites of potential cell to cell interaction. Vesicles were heterogeneous in size, typically 200–500 nm, with occasional enlarged structures measuring approximately 2 µm in diameter (**Fig.** 5, Panels 4A and

4B), consistent with vesicle coalescence or fusion. Pigment density ranged from intensely black to lightly pigmented gray (**Fig.** 5, Panels 2B, 3A, 4B), indicating variability in pigment maturation, storage, or turnover both among cells and within individual processes. Vesicles of differing pigment intensity (approximately 0.25–0.4 µm diameter) coexisted within the same dendritic branches (**Fig.** 5, Panels 2B and 4B, red arrows), supporting asynchronous vesicular maturation within single interstitial cells.

TEM Imaging of Pigmented SAN Areas

In mammals, melanin and neuromelanin are two major endogenous biological pigments associated with intracellular production and storage in membrane-bound vesicles. Because confocal microscopy has limited optical resolution and cannot reliably resolve the membranes surrounding these pigmented vesicles, we extended our investigation of pigmented areas of the sinoatrial node (SAN) using transmission electron microscopy (TEM), which allowed us to examine the ultrastructural details of the interstitial cells at higher resolution. Based on the observed dendritic and amoeboid morphologies and the presence of intracellular pigmented vesicles, we describe these S100B$^+$ interstitial cells as *melanocyte-like S100B$^+$ interstitial cells* or *melanocyte-like cells*. This terminology reflects their morphological and ultrastructural features and vesicular pigment content, without implying that their melanocytic identity has been definitively established.

To correlate light microscopy observations with nanoscale ultrastructural features, we used a sequential same-section workflow. Semi-thin longitudinal sections of pigmented SAN tissue were first examined by light microscopy after toluidine blue staining to identify melanocyte-like interstitial cells containing intracellular pigmented vesicles

(**Fig.** 6, panel A). The same sections were then examined by transmission electron microscopy (TEM) to resolve the ultrastructure of these cells and their vesicular contents at higher resolution (**Fig.** 6, panels B–D). This approach enabled comparison of cellular features identified by light microscopy with their ultrastructural characteristics revealed by TEM.

Telopodes appeared more morphologically variable in confocal images than in TEM. Nevertheless, a subset of cells detected by both techniques exhibited features consistent with telocytes (Mitrofanova et al. 2018). For clarity, we use "telocytes" in the TEM section as a synonym for interstitial dendritic cells. Figure 6 illustrates pigmented telocytes and amoeboid interstitial cells colocalized within the central SAN. The telocyte soma contains a cluster of pigmented vesicles (**Fig.** 6, Panel B, green arrow) from which a telopode extends. The telopode alternates between thin podomers and bead-like podoms. Podoms (yellow stars in **Fig.** 6B–D) contained both pigmented and unpigmented vesicles. Pigmented vesicles were also present within podomers, indicating somatic origin and directed transport along telopodes toward distal regions for local signaling or intercellular communication.

TEM reconstructions revealed contact sites between telocytes and pacemaker cells formed by dilated telopodal endfeet or varicosities densely packed with pigmented vesicles (**Fig.** 7, Panels B and C). Their organization resembled neuronal synapses, with vesicle-filled telopodal endfeet analogous to presynaptic compartments and adjacent pacemaker cells to postsynaptic counterparts, supporting their designation as synaptic-like contacts. Similar contacts were observed between telocytes and peripheral nerves

(**Fig.** 7, Panel D), where telopodal endfeet partially enwrapped nerves, forming a microenvironment suitable for vesicular release.

Compared with dendritic telocytes, amoeboid interstitial cells (**Fig.** 8, panel A) exhibited a contrasting morphology, with rounded or irregularly shaped somata and short cytoplasmic extensions. Their cytoplasm was densely filled with pigmented vesicles of varying sizes and electron densities, distributed throughout the cell without apparent polarization, consistent with a storage-like organization. A tiled image of an amoeboid interstitial cell shows pigmented vesicles assembled into multivesicular bodies or clusters enclosed within a vesicular membrane (**Fig.** 9, Panel A). These clusters contained two to seven vesicles, and a release site of such a multivesicular complex into the interstitial space is indicated by a yellow star. Pigmented vesicles with heterogeneous coats were also present within the interstitial space of the SAN (**Fig.** 9, Panel B).

Intracellular vesicles in both telocytes and amoeboid interstitial cells ranged from approximately 100 nm to approximately 500 nm and exhibited homogeneous or heterogeneous electron densities (**Fig.** 6–9). Both spherical and elongated oval vesicles were observed within the same cell type, without consistent association between vesicle shape, size, and electron density. Some cells contained a dominant vesicle population with homogeneous electron-dense cargo.

Pigmented vesicles spanning 100–500 nm within individual interstitial cells are consistent with sequential maturation stages. An initial stage showed vesicles with largely empty lumens and minimal electron-dense cargo (**Fig.** 8, Panel B). A second stage exhibited reduced intravesicular space with increased cargo density (**Fig.** 8, Panel C). A third stage was suggested by linear arrangements of vesicles with progressively

increasing diameters (approximately 150–500 nm), indicating continued growth and cargo accumulation (**Fig.** 8, Panel D). This ordered arrangement suggests coordinated vesicular maturation rather than stochastic assembly.

Endo–Epicardially Dispersed EdU Incorporation Lacking Regional Compartmentalization

We employed EdU labeling to assess mitotic activity within the SAN. EdU-positive nuclei were scattered throughout the $HCN4^+$ meshwork from head to tail (**Fig.** 10A–C). Colocalization of EdU and DAPI confirmed nuclear identity. No EdU-labeled nuclei were detected within $HCN4^+$ pacemaker cells; all labeled nuclei were confined to interstitial spaces.

Semi-automatic detection of nuclei within a 600 × 600 µm area enabled total nuclear counts and calculation of EdU labeling indices across three SAN regions (**Fig.** 10D). The proportion of EdU-labeled nuclei was low (5–7%), with mean labeling indices of approximately 6.7% in the head, approximately 5.7% in the body, and approximately 6.1% in the tail. No significant regional differences were detected (one-way ANOVA: $F = 0.16$, $P = 0.86$), and pairwise *t*-tests confirmed the absence of significant differences (all $P > 0.55$). Analysis of EdU^+ nuclei counts likewise showed no regional variation (one-way ANOVA, $F(2,17) = 1.18$, $P = 0.33$). Mean counts were 32.7 ± 4.8 ($n = 7$) in the head, 24.0 ± 5.0 ($n = 6$) in the body, and 23.0 ± 5.1 ($n = 7$) in the tail. These findings indicate uniformly low proliferative activity across SAN regions relative to the total number of DAPI-labeled nuclei within the corresponding regions of interest.

To assess spatial distribution along the endo–epicardial axis, Z-stack datasets were analyzed by orthogonal sectioning to generate three-dimensional reconstructions of

EdU⁺ nuclei. A layered arrangement resembling germinative zones (e.g., basal epidermis or intestinal crypts) was not observed. Instead, three distribution patterns were identified (**Fig.** 11): epicardial polarization (Panel A), endocardial polarization (Panel B), and homogeneous distribution across the axis (Panel C). Although Figure 11 shows examples from the head, body, and tail, all three patterns occurred throughout these regions. Thus, the SAN lacks a dominant proliferative zone despite prior reports of progenitor enrichment near the epicardial surface (Miao et al. 2025; Quijada et al. 2020), suggesting that proliferative activity is spatially dispersed rather than regionally compartmentalized within the node.

S100B⁺ Proliferative Nests and the Spatial Distribution of EdU⁺ Interstitial Cells

Within both morphological groups of S100B⁺ interstitial cells dendritic and amoeboid two subgroups were distinguished: cells containing intracellular pigmented vesicles and thus exhibiting melanocyte-like features, and cells lacking these vesicles or containing only very low levels of intracellular vesicles. EdU⁺ nuclei were detected in both morphological groups, indicating that these cells had undergone DNA synthesis associated with cell proliferation (**Fig.** 12 and 13).

We identified a previously undescribed cytoarchitecture of S100B⁺ cells in the SAN (**Fig.** 12A, B). Based on their visual appearance, we refer to these structures as *S100B⁺ proliferative nests*. These nests at higher resolution appeared as elongated, ovoid multicellular structures containing two or more EdU⁺ nuclei (**Fig.** 12C–F). Perinuclear cytoplasmic contours were discernible within the nests, with closely apposed nuclei separated by thin cytoplasmic bands and enclosed by cellular membrane. However, we

cannot exclude the presence of individual plasma membranes between adjacent nuclei. Because of the limited spatial resolution of confocal microscopy, these membrane boundaries could not be definitively resolved, leaving uncertain whether the nuclei within each nest belong to separate cells or share a common cytoplasmic compartment.

Orthogonal views of three-dimensional reconstructions confirmed the spatial localization of EdU^+ nuclei within $S100B^+$ nests in both non-pigmented regions (**Fig.** 12) and pigmented regions (**Fig.** 13). In the overlaid fluorescence and transmitted-light images, pigment appears black because it is visible in the transmitted-light images. Pigment may also absorb emitted fluorescence, reducing the detectable signal from the fluorophores.

Dense intracellular pigment obscured cellular boundaries, even at higher imaging resolution, and restricted fluorescence detection largely to the nuclei, limiting detailed examination of nest cytoarchitecture (**Fig.** 13B–D). Nevertheless, double EdU^+ nuclei were observed within pigmented areas. In regions with lower pigment density, pigmented cytoplasmic vesicles surrounding EdU^+ nuclei were visible (**Fig.** 13D–G). $S100B^+$ nests were observed in both the head and body regions of the SAN, with no apparent regional preference. Their sporadic distribution suggests that the absence of nests in the tail region of the $HCN4^+$ meshwork may reflect the timing of observation: nests may not yet have formed or progressed to a detectable stage in this region. Thus, their absence in the tail should not be interpreted as evidence that nest formation is restricted to particular SAN regions. Quantification of EdU^+ nuclei in 11 nests from three SAN preparations showed a mean of 2.8 ± 1.2 nuclei per nest (median = 2). Most nests were small: 7 of 11 (64%) contained two EdU^+ nuclei, three contained four nuclei, and one contained five (three

EdU$^+$). Thus, proliferative nests typically generate limited numbers of closely apposed daughter cells.

Based on the presence of S100B$^+$ nests containing EdU$^+$ nuclei and the observation of EdU$^+$ dendritic and amoeboid cells within clusters and as isolated cells several hundred micrometers away from the nests, we propose the following hypothetical sequence of events: (1) proliferation of S100B$^+$ interstitial cells within nests; (2) release of amoeboid cells from the nests; (3) their possible dispersal away from the nests; and (4) their occurrence as isolated cells or within more distant clusters. This hypothetical model could explain the apparently random patterns of EdU labeling observed among SAN interstitial cells (**Fig.** 12–14).

Close examination of the images of S100B$^+$ nests revealed morphological details that are consistent with our hypothesis. Because cellular division has been extensively documented, we examined the cytoarchitecture of EdU$^+$/S100B$^+$ nests for features potentially associated with cell division and separation. We identified a range of nest configurations, from compact structures with closely apposed nuclei and minimal perinuclear cytoplasm to nests with expanded cytoplasmic compartments, emerging extensions, and progressively restricted cytoplasmic continuity between neighboring nuclei. These morphological features may represent stages of cellular separation, although static images cannot establish the temporal sequence.

1. Compact S100B$^+$ nests containing closely apposed EdU$^+$ nuclei with minimal perinuclear cytoplasm, producing an “egg-like” appearance (Fig. 12A, C; 13B).

2. Expansion of extranuclear cytoplasm with emerging cytoplasmic extensions, accompanied by increasing separation of nuclei and thinning of the shared cytoplasmic compartment within the nest (Fig. 12F; 13D).
3. Restriction of cytoplasmic continuity to narrow bridges, with progressively distinct cytoplasmic domains (Fig. 12G).
4. Separated adjacent S100B$^+$ cells containing EdU$^+$ nuclei (Fig. 14A, B).

Although static images cannot establish a temporal sequence, we observed solitary S100B$^+$/EdU$^+$ cells with an amoeboid morphology (Fig. 13E, F; Fig. 14C, D). This morphology is consistent with a potential migratory phenotype and raises the possibility that amoeboid cells may disperse from the nests. A subsequent stage in our proposed model would involve the growth and organization of these cells over time. This process could result in configurations frequently observed in our preparations: two or more closely positioned S100B$^+$/EdU$^+$ cells with dendritic or amoeboid morphologies, either with (Fig. 13H) or without (Fig. 14B) pigmented vesicles, within the HCN4$^+$ pacemaker meshwork. The clearly defined cellular boundaries in these configurations are consistent with distinct cellular identities following nest disassembly. An example is shown in Figure 14E, where 17 S100B$^+$ cells formed an irregular plexus within the HCN4$^+$ meshwork. Four of these cells contained EdU$^+$ nuclei (yellow arrows), including a S100B$^+$/EdU$^+$ nest (white arrow). The coexistence of S100B+/EdU$^+$ dendritic cells within an irregular plexus and a nearby S100B$^+$/EdU$^+$ nest provides spatial evidence consistent with our proposed model of nest-associated proliferation, cellular separation, and subsequent redistribution within the surrounding interstitial space.

DISCUSSION

S100B$^+$ Interstitial Cells and the Dynamic Assembly of SAN Tissue Architecture

Our study identifies S100B$^+$ interstitial cells of the sinoatrial node (SAN) as a structurally heterogeneous population with proliferative activity. The presence of nest-like proliferative units, together with EdU incorporation within the nests and EdU-positive nuclei among dispersed S100B$^+$ interstitial cells, suggests that these nests may serve as localized sites of cell proliferation. We hypothesize that, following cell division and separation within the nests, S100B$^+$ interstitial cells disperse toward more distant locations within the SAN. This hypothesis is further supported by the observation of apparent stages of cellular separation from the nests and by the distinct categories of spatial distribution patterns of S100B$^+$ cells: patchy, contiguous, and dispersed, observed in SAN preparations from different mice. Notably, each SAN preparation exhibited a unique distribution pattern, with variation among preparations within each of these categories. This variability suggests that the observed patterns do not represent uniform or stereotyped arrangements, but may reflect the dynamic processes underlying the proliferation and dispersal of S100B$^+$ interstitial cells within the SAN.

According to this model, localized proliferation within nests is followed by cell dispersal throughout the HCN4$^+$ pacemaker cell meshwork, potentially contributing to the distribution of dendritic and amoeboid interstitial populations. Notably, we did not observe extensive or anatomically restricted regions of proliferative activity, such as those confined to endothelial or epithelial compartments. Instead, nests occurred at scattered locations throughout the SAN. However, the close apposition of nuclei within the nests and the inability to resolve boundaries between adjacent cells limited our ability to

establish the precise sequence of cell separation and subsequent migration. Thus, although this model may explain the observed proliferative activity and morphological diversity of $S100B^+$ interstitial cells, direct tracking of individual cells will be required to establish the proposed mechanism.

A second major finding concerns intracellular pigment in $S100B^+$ interstitial cells. Pigment-containing cells were also observed within proliferative nests, raising the possibility that pigment is retained during cell proliferation and distributed among different SAN morphotypes through subsequent cell dispersal. Transmission electron microscopy confirmed the presence of pigment-containing intracellular vesicles and vesicular structures in the interstitial space. These observations suggest that pigment-containing vesicles may be released from $S100B^+$ cells into the extracellular environment.

Parallels in Tissue Complexity Between the SAN and Brain

The cellular complexity of the SAN, reflected in the expression of S100B by three distinct cell types, together with the multifunctional roles of S100B in processes including cell migration, proliferation, and Ca^{2+} homeostasis, prompted us to consider parallels between SAN cytoarchitecture and brain tissue architecture. The anatomical interactions between $HCN4^+$ pacemaker cells and $S100B^+$ amoeboid and dendritic interstitial cells may provide pathways for functional communication. Vesicles observed in confocal and TEM images could potentially be delivered to pacemaker cells and modify their pacemaker activity by altering intracellular Ca^{2+} kinetics.

As discussed above, we hypothesize that proliferation and subsequent dispersal of $S100B^+$ interstitial cells may contribute to the formation of distinct millimeter-scale SAN tissue morphotypes. Together with the $GFAP^+/S100B^+$ peripheral glial web described

previously (Bychkov et al. 2022), these cellular arrangements (**Figure 1 supplement**) establish a spatially heterogeneous S100B$^+$ cellular environment within the HCN4$^+$ meshwork extending from the superior to the inferior vena cava. Regions containing greater numbers of S100B$^+$ interstitial cells may represent sites of increased local S100B availability, whereas other regions may contain fewer such cells. The glial web may provide an additional potential source of S100B through secretion. However, the relative contributions of these cellular populations to extracellular S100B availability remain to be determined.

Another possibility is that HCN4$^+$ pacemaker cells produce and release signals that influence the spatial distribution of S100B$^+$ interstitial cells. Thus, the observed distribution may reflect reciprocal interactions between these two cell populations. Because S100B expression and melanin-like pigmentation are features associated with melanocytes, the pigment-containing S100B$^+$ interstitial cells observed in our study exhibit certain melanocyte-like features. These cells may be responsive to signaling factors of neuronal origin. Lim and coauthors (Lim et al. 2024) reported that single-cell transcriptome analysis identified a broad repertoire of neuron-associated genes in SAN pacemaker cells. Although this finding does not establish a mechanism by which pacemaker cells regulate the spatial distribution of S100B$^+$ interstitial cells, it raises the possibility that signaling pathways associated with these genes may contribute to their spatial organization within the SAN.

Whether pacemaker cell signals recruit or influence the distribution of S100B$^+$ interstitial cells remains an open question. These proposed interactions draw on selected morphological and molecular parallels with neuronal systems and do not imply that SAN

tissue assembly follows the same mechanisms as neuronal tissue development. Nevertheless, the distinct cytoarchitectures of the SAN glial web and S100B$^+$ interstitial cell populations, together with the molecular and phenotypic features that distinguish pacemaker cells from contractile cardiac myocytes, suggest that the SAN shares certain organizational and molecular characteristics with neuronal systems. In this context, the hypothesis that the SAN is the “central brain of the heart” (Bychkov et al. 2022; Donald and Lakatta 2023) can be understood as a functional analogy emphasizing its role in initiating and coordinating rhythmic cardiac contraction.

Proliferation, Dispersal, and Phenotypic Diversity of S100B$^+$ Interstitial Cells.

The amoeboid and dendritic phenotypes are generally associated with distinct cellular functions. Amoeboid S100B$^+$ interstitial cells exhibit rounded, oval, or irregular morphologies, with cytoplasmic extensions that generally do not exceed the largest diameter of the cell soma. Such extensions, which vary in size, are features commonly associated with migratory behavior (Graziani et al. 2022). In contrast, dendritic S100B$^+$ cells have small somata, approximately 5–10 µm in diameter, and elongated, branched processes that can reach lengths of up to 100 µm, forming unipolar, bipolar, or multipolar arborizations with spine-like protrusions.

The close apposition of interstitial cell processes and pacemaker cell membranes within micrometer-scale spaces provides an anatomical basis for potential localized interactions with pacemaker cells and nerves. Such arrangements may permit compartmentalized modulation of cellular activity. Indeed, localized Ca^{2+} transients have been documented in dendritic processes of melanocytes in response to endothelin-1 and acetylcholine (Belote and Simon 2020), supporting the possibility of microdomain-level

signaling in dendritic processes, although its role in SAN pacemaker activity remains to be established.

The clustered distribution of amoeboid and dendritic S100B$^+$ cells, together with EdU$^+$ proliferative nests and dispersed S100B$^+$ cells containing EdU-labeled nuclei, raises the possibility that the SAN interstitium undergoes ongoing cellular turnover or remodeling. Within the nests, the nuclei of dividing cells are closely packed, and the intervening cell membranes cannot be distinguished at confocal microscopy resolution. This cellular arrangement resembles proliferative and migratory cellular assemblies described in neural crest development (Smith-Thomas and Fawcett 1989), axonal regeneration (Wang et al. 1996), and melanocytic lesions (Balu et al. 2014; Luzar et al. 2020; Van Raamsdonk and Deo 2013). The coexistence of proliferative nests, transitional morphological forms, and dispersed EdU$^+$ cells is consistent with a possible process of local cell proliferation followed by dispersal. Whether this process represents steady-state cellular renewal or adaptive tissue remodeling remains unresolved.

One hypothesis is that amoeboid and dendritic interstitial cells originate from the same proliferative nests and subsequently disperse to different locations within the SAN, where they acquire distinct mature phenotypes. This hypothesis draws an analogy with cell dispersal and differentiation during the development of neuronal tissues, where cellular fate can be influenced by the local microenvironment. For example, the extracellular matrix has been reported to influence neural crest cell fate decisions (Sun et al. 2023; Zhu et al. 2019). Although these findings concern neural crest development rather than SAN interstitial cells, they raise the possibility that extracellular matrix and other local microenvironmental cues contribute to phenotypic diversification within the

SAN. The presence of transitional morphological forms is consistent with the possibility that dendritic cells arise from smaller amoeboid precursors, although this developmental relationship has not been established. Alternatively, distinct types of proliferative nests may give rise separately to amoeboid and dendritic cells. However, we did not identify morphological features that would allow us to distinguish between these possibilities.

Pigmented Vesicles and Phenotypic Diversity of S100B$^+$ Interstitial Cells

Intracellular pigment is a characteristic feature of melanocytes. The presence of pigmented vesicles in S100B$^+$-immunoreactive dendritic and amoeboid interstitial cells led us to describe these cells as *melanocyte-like cells*. Correlative confocal and transmission electron microscopy (TEM) allowed us to examine these cells at different spatial resolutions.

TEM revealed vesicles of different sizes and electron densities, consistent with progressive maturation into densely condensed bodies and multivesicular aggregates. In dendritic cells, pigmented vesicles were observed within the somata and along telopodes, suggesting intracellular transport toward distal cellular processes. Amoeboid cells frequently contained densely packed vesicles at different apparent stages of maturation, often organized into multivesicular bodies. This accumulation may indicate that vesicles are stored within the cells rather than released immediately after formation. Coated vesicles observed in the interstitial space near amoeboid cells and dendritic cell podoms and podomers are consistent with the possibility of vesicular secretion. Vesicles were also found in the interstitial space near synaptic-like contacts involving telocyte telopodal endfeet and pacemaker cells, including regions adjacent to pacemaker cell membranes.

These observations provide an anatomical basis for potential vesicle-mediated paracrine signaling.

To our knowledge, this represents the first ultrastructural demonstration of pigmented vesicles in cardiac interstitial cells. Although pigmented vesicles have been described in skin telocytes (Díaz-Flores et al. 2014), previous reports of SAN telocytes did not document pigmentation. The pigmented $S100B^+$ dendritic cells identified here may therefore broaden the recognized phenotypic spectrum of SAN interstitial cells. To our knowledge, amoeboid $S100B^+$ interstitial cells have also not been previously described in the SAN.

The dendritic $S100B^+$ cells exhibited morphological features resembling those of SAN telocytes described by Mitrofanova et al. (2018), including telopodes with alternating podoms and podomers. However, not all dendritic interstitial cells observed by confocal microscopy could be classified as telocytes. Only a subset displayed characteristic telopodal morphology and branching patterns consistent with those observed in TEM images. Other dendritic cells, with thicker processes or longer and atypical branching patterns, may represent a distinct interstitial cell subpopulation or morphological adaptations of telocytes to their local environment.

Together, these findings raise the possibility that pigment and S100B may be released together or through coordinated processes and may influence local cellular functions, including Ca^{2+} homeostasis, redox regulation, immune responses, and Ca^{2+}-dependent vesicular release (Bychkov et al. 2022; Davey et al. 2001; Leite et al. 2023; Alegre et al. 2016; Benito-Martín et al. 2023). Finally, we identified $S100B^+$ dendritic and amoeboid interstitial cells both with and without pigmented vesicles. This observation has

two possible explanations. First, these cells may represent phenotypically similar populations that differ in their ability to produce pigment. Alternatively, pigment production may be cyclical or may occur in response to external stimuli.

Conclusions: S100B$^+$ Interstitial Cell Proliferation in the Context of Neural Crest Biology

The co-occurrence of S100B expression and pigment production in SAN interstitial cells raises questions about their developmental origin. Our hypothesis is that S100B$^+$ melanocyte-like cells in the SAN may originate from the neural crest. It is based on their expression of S100B, a marker associated with glial cells and melanocytes, and the presence of pigment, which is consistent with the pigment-producing phenotype of melanocytes (Adameyko et al. 2012; Hernández-Ortega et al. 2024). Because both glial cells and melanocytes can originate from the neural crest, these features provide a rationale for hypothesizing that S100B$^+$ pigment-containing interstitial cells in the SAN may also be neural crest-derived. However, this hypothesis remains to be tested, as these features alone do not establish the cells' developmental origin.

In the heart cardiac neural crest cells contribute to the conduction system and express neuronal and melanocytic markers (Nakamura et al. 2006). The phenotypic variability of S100B$^+$ melanocyte-like cells is consistent with the phenotypic plasticity of neural crest-derived melanocytes and glia, which can also transdifferentiate under defined conditions (Dupin et al. 2000; Dupin et al. 2003). This similarity does not establish their origin but provides a conceptual framework for investigating the glial-like and melanocyte-like features of these cells.The melanosome-like vesicles further links these cells to the glia melanocyte axis (Dupin et al. 2003; Dupin and Sommer 2012; Petersen

and Adameyko 2017). The reported functions of cutaneous melanocytes, including endocrine signaling and circadian entrainment (Bi et al. 2025; Chen et al. 2022; Chhabra et al. 2026), and extracutaneous melanocytes, including sensory hair cell support (Nayak et al. 2026), choroidal homeostasis (Cioanca et al. 2021), and myocardial redox balance (Levin et al. 2009), suggest potential functional directions for future studies of pigmented SAN interstitial cells.

A second unresolved question concerns the origin of the cells that proliferate and create cytoarchitecture of nests. Evidence that neural crest cells can generate melanocytes and persist in the heart as multipotent populations supports the possibility that they give rise to the proliferative nests in different tissues including SAN (Dupin and Sommer 2012; Le Douarin et al. 2004; Soldatov et al. 2019; Mehrotra et al. 2023; Nakamura et al. 2006; Tomita et al. 2005). Alternatively, Schwann cell precursors accompanying peripheral nerves can generate melanocytes and undergo glia–melanocyte interconversion (Kastriti et al. 2022; Rizvi et al. 2002; Gacem et al. 2020). Pigmented cardiac cells have also been reported in the atrium, septum, valves, veins, and SAN artery (Levin et al. 2009; Mjaatvedt et al. 2005; Yajima and Larue 2008).

Together, our findings identify S100B$^+$ interstitial cells with proliferative activity, pigmented vesicles, and potential secretory features within the HCN4$^+$ pacemaker meshwork. These cells may represent a dynamic component of the pacemaker microenvironment. S100B$^+$ cells are present in the developing SAN at embryonic day 16 (E16), in close proximity to HCN4$^+$ pacemaker cells, and persist in aged mice up to at least 30 months (Supplemental Figure 2). Although S100B has been reported to decrease heart rate, the broader functional roles and developmental origins of these cells remain

unresolved (Bychkov et al. 2022). Their proliferative capacity, neural crest-related characteristics, and pigment-associated vesicles support further investigation of their potential contributions to SAN development, function and age-related remodeling.

ACKNOWLEDGMENTS

The authors thank the National Institute on Aging Intramural Research Program for institutional support. ChatGPT version 5.2, an AI language model developed by OpenAI, was used by the author to review the English grammar, spelling, and overall language quality of all sections of this paper to improve clarity and readability. The content was checked for linguistic accuracy while preserving the original meaning.

FUNDING

This research was supported by the Intramural Research Program of the National Institutes of Health (NIH). The contributions of the NIH author(s) are considered Works of the United States Government. The findings and conclusions presented in this paper are those of the author(s) and do not necessarily reflect the views of the NIH or the U.S. Department of Health and Human Services.

DISCLOSURES

The authors have reported that they have no relationships relevant to the contents of this paper to disclose.

REFERENCES

1. Adameyko I, Lallemend F, Furlan A et al (2012) Sox2 and Mitf cross-regulatory interactions consolidate progenitor and melanocyte lineages in the cranial neural crest. Development 139:397–410. https://doi.org/10.1242/dev.065581
2. Alegre E, Zubiri L, Perez-Gracia JL, González-Cao M, Soria L, Martín-Algarra S, González A (2016) Circulating melanoma exosomes as diagnostic and prognosis biomarkers. Clin Chim Acta. 454:28–32. https://doi.org/10.1016/j.cca.2015.12.031
3. Anderson RH, Yanni J, Boyett MR, Chandler NJ, Dobrzynski H (2009) The anatomy of the cardiac conduction system. Clin Anat. 22:99–113. https://doi.org/10.1002/ca.20700
4. Balu M, Kelly KM, Zachary CB, Harris RM, Krasieva TB, König K, Durkin AJ, Tromberg BJ (2014) Distinguishing between benign and malignant melanocytic nevi by in vivo multiphoton microscopy. Cancer Res. 74:2688–97. https://doi.org/10.1158/0008-5472.CAN-13-2582
5. Belote RL, Simon SM (2020) Ca2+ transients in melanocyte dendrites and dendritic spine-like structures evoked by cell-to-cell signaling. J Cell Biol. 219:e201902014. https://doi.org/10.1083/jcb.201902014
6. Benito-Martín A, Jasiulionis MG, García-Silva S (2023) Extracellular vesicles and melanoma: New perspectives on tumor microenvironment and metastasis. Front Cell Dev Biol. 10:1061982. https://doi.org/10.3389/fcell.2022.1061982
7. Bi O, Caballero-Lima D, Sikkink S, Westgate G, Kauser S, Elies J, Thornton MJ (2025) Do Melanocytes Have a Role in Controlling Epidermal Bacterial Colonisation and the Skin Microbiome? Exp Dermatol. 34:e70071. https://doi.org/10.1111/exd.70071

8. Bianchi R, Kastrisianaki E, Giambanco I, Donato R (2011) S100B protein stimulates microglia migration via RAGE-dependent up-regulation of chemokine expression and release. J Biol Chem. 286:7214–26. https://doi.org/10.1074/jbc.M110.169342
9. Bresnick AR, Weber DJ, Zimmer DB (2015) S100 proteins in cancer. Nat Rev Cancer. 15:96–109. https://doi.org/10.1038/nrc3893
10. Bychkov R, Juhaszova M, Tsutsui K, Coletta C, Stern MD, Maltsev VA, Lakatta EG (2020) Synchronized Cardiac Impulses Emerge From Heterogeneous Local Calcium Signals Within and Among Cells of Pacemaker Tissue. JACC Clin Electrophysiol. 6:907–931. https://doi.org/10.1016/j.jacep.2020.06.022
11. Bychkov R, Juhaszova M, Calvo-Rubio Barrera M, Donald LAH, Coletta C, Shumaker C, Moorman K, Sirenko ST, Maltsev AV, Sollott SJ, Lakatta EG (2022) The Heart's Pacemaker Mimics Brain Cytoarchitecture and Function: Novel Interstitial Cells Expose Complexity of the SAN. JACC Clin Electrophysiol. 8:1191–1215. https://doi.org/10.1016/j.jacep.2022.07.003
12. Chen YY, Liu LP, Zhou H, Zheng YW, Li YM (2022) Recognition of Melanocytes in Immuno-Neuroendocrinology and Circadian Rhythms: Beyond the Conventional Melanin Synthesis. Cells. 11:2082. https://doi.org/10.3390/cells11132082
13. Chhabra Y, Jagirdar KR, Galluzzi L (2026) Melanosomes support immune evasion in melanoma. Cell Mol Immunol. https://doi.org/10.1038/s41423-026-01393-z
14. Cioanca AV, Wu CS, Natoli R, Conway RM, McCluskey PJ, Jager MJ, Sitiwin EI, Eamegdool SS, Madigan MC (2021) The role of melanocytes in the human choroidal microenvironment and inflammation: Insights from the transcriptome. Pigment Cell Melanoma Res. 34:928–945. https://doi.org/10.1111/pcmr.12972

15. Davey GE, Murmann P, Heizmann CW (2001) Intracellular Ca2+ and Zn2+ levels regulate the alternative cell density-dependent secretion of S100B in human glioblastoma cells. J Biol Chem. 276:30819–26. https://doi.org/10.1074/jbc.M103541200

16. Donald L, Lakatta EG (2023) What makes the sinoatrial node tick? A question not for the faint of heart. Philos Trans R Soc Lond B Biol Sci. 378:20220180. https://doi.org/10.1098/rstb.2022.0180

17. Donato R, Sorci G, Riuzzi F et al (2009) S100B's double life: intracellular regulator and extracellular signal. Biochim Biophys Acta 1793:1008–1022. https://doi.org/10.1016/j.bbamcr.2008.11.009

18. Donato R, Cannon BR, Sorci G, Riuzzi F, Hsu K, Weber DJ, Geczy CL (2013) Functions of S100 proteins. Curr Mol Med. 13:24–57. https://pmc.ncbi.nlm.nih.gov/articles/PMC3707951/

19. Dupin E, Glavieux C, Vaigot P, Le Douarin NM (2000) Endothelin 3 induces the reversion of melanocytes to glia through a neural crest-derived glial-melanocytic progenitor. Proc Natl Acad Sci U S A 97:7882–7887. https://doi.org/10.1073/pnas.97.14.7882

20. Dupin E, Real C, Glavieux-Pardanaud C, Vaigot P, Le Douarin NM (2003) Reversal of developmental restrictions in neural crest lineages: transition from Schwann cells to glial-melanocytic precursors in vitro. Proc Natl Acad Sci U S A 100:5229–5233. https://doi.org/10.1073/pnas.0831229100

21. Dupin E, Sommer L (2012) Neural crest progenitors and stem cells: from early development to adulthood. Dev Biol. 366:83–95. https://doi.org/10.1016/j.ydbio.2012.02.035

22. Díaz-Flores L, Gutiérrez R, García MP, Sáez FJ, Aparicio F, Díaz-Flores L Jr, Madrid JF (2014) Uptake and intracytoplasmic storage of pigmented particles by human CD34+ stromal cells/telocytes: endocytic property of telocytes. J Cell Mol Med. 18:2478–87. https://doi.org/10.1111/jcmm.12437

23. Gacem N, Kavo A, Zerad L, Richard L, Mathis S, Kapur RP, Parisot M, Amiel J, Dufour S, de la Grange P, Pingault V, Vallat JM, Bondurand N (2020) ADAR1 mediated regulation of neural crest derived melanocytes and Schwann cell development. Nat Commun. 11:198. https://doi.org/10.1038/s41467-019-14090-5

24. Graziani V, Rodriguez-Hernandez I, Maiques O, Sanz-Moreno V (2022) The amoeboid state as part of the epithelial-to-mesenchymal transition programme. Trends Cell Biol 32:228–242. https:/doi.org/10.1016/j.tcb.2021.10.004

25. Hernández-Ortega K, Canul-Euan AA, Solis-Paredes JM, Borboa-Olivares H, Reyes-Muñoz E, Estrada-Gutierrez G, Camacho-Arroyo I (2024) S100B actions on glial and neuronal cells in the developing brain: an overview. Front Neurosci 18:1425525. https://doi.org/10.3389/fnins.2024.1425525

26. Kastriti ME, Faure L, Von Ahsen D, Bouderlique TG, Boström J, Solovieva T, Jackson C, Bronner M, Meijer D, Hadjab S, Lallemend F, Erickson A, Kaucka M, Dyachuk V, Perlmann T, Lahti L, Krivanek J, Brunet JF, Fried K, Adameyko I (2022) Schwann cell precursors represent a neural crest-like state with biased multipotency. EMBO J. 41:e108780. https://doi.org/10.15252/embj.2021108780

826 27. Lakatta EG, Maltsev VA, Vinogradova TM (2010) A coupled SYSTEM of
827 intracellular Ca^{2+} clocks and surface membrane voltage clocks controls the
828 timekeeping mechanism of the heart's pacemaker. Circ Res 106:659–673.
829 https://doi.org/10.1161/CIRCRESAHA.109.206078
830 28. Le Douarin NM, Creuzet S, Couly G, Dupin E (2004) Neural crest cell plasticity
831 and its limits. Development. 131:4637–50. https://doi.org/10.1242/dev.01350
832 29. Leite MC, Galland F, Guerra MC, Rodrigues L, Taday J, Monteforte PT, Hirata H,
833 Gottfried C, Donato R, Smaili S, Gonçalves CA (2023) Astroglial S100B Secretion Is
834 Mediated by Ca2+ Mobilization from Endoplasmic Reticulum: A Study Using Forskolin
835 and DMSO as Secretagogues. Int J Mol Sci. 24:16576.
836 https://doi.org/10.3390/ijms242316576
837 30. Levin MD, Lu MM, Petrenko NB, Hawkins BJ, Gupta TH, Lang D, Buckley PT,
838 Jochems J, Liu F, Spurney CF, Yuan LJ, Jacobson JT, Brown CB, Huang L, Beermann
839 F, Margulies KB, Madesh M, Eberwine JH, Epstein JA, Patel VV (2009) Melanocyte-
840 like cells in the heart and pulmonary veins contribute to atrial arrhythmia triggers. J Clin
841 Invest. 119:3420–36. https://doi.org/10.1172/JCI39109
842 31. Lim AA, Pouyabahar D, Ashraf M, Huang K, Lohbihler M, Murareanu BM, Chang
843 ML, Kwan M, Alibhai FJ, Tran T, Mazine A, Laflamme MA, Bader GD, Laksman Z,
844 Protze S (2024) Single-cell transcriptome analysis reveals CD34 as a marker of human
845 sinoatrial node pacemaker cardiomyocytes. Nat Commun. 15:10206.
846 https://doi.org/10.1038/s41467-024-54337-4
847 32. Luzar B, Billings SD, de la Fouchardiere A, Pissaloux D, Alberti L, Calonje E (2020)
848 Compound Clear Cell Sarcoma of the Skin-A Potential Diagnostic Pitfall: Report of a

Series of 4 New Cases and a Review of the Literature. Am J Surg Pathol. 44:21–29. https://doi.org/10.1097/PAS.0000000000001404

33. Mehrotra P, Ikhapoh I, Lei P, Tseropoulos G, Zhang Y, Wang J, Liu S, Bronner ME, Andreadis ST (2023) Wnt/BMP Mediated Metabolic Reprogramming Preserves Multipotency of Neural Crest-Like Stem Cells. Stem Cells. 41:287–305. https://doi.org/10.1093/stmcls/sxad001

34. Miao L, Nusrat A, Li J, Yin C, Lu Y, Kuang X, Sun D, Lo E, Song R, Huang W, Long X, McConnell BK, Singer HA, Schwartz RJ, Gunaratne P, Fan ZC, Kumar A, Zhou B, Munshi N, Evans SM, Wu M (2025) Distinct populations of vascular smooth muscle and sinoatrial progenitors are localized adjacent to pro-epicardium. Cell Rep. 44:116580. https://doi.org/10.1016/j.celrep.2025.116580

35. Michetti F, Corvino V, Geloso MC et al (2012) The S100B protein in biological fluids: more than a lifelong biomarker of brain distress. J Neurochem 120:644–659. https://doi.org/10.1111/j.1471-4159.2011.07612.x

36. Michetti F, D'Ambrosi N, Toesca A, Puglisi MA, Serrano A, Marchese E, Corvino V, Geloso MC (2019) The S100B story: from biomarker to active factor in neural injury. J Neurochem. 148:168–187. https://doi.org/10.1111/jnc.14574

37. Michetti F, Clementi ME, Di Liddo R, Valeriani F, Ria F, Rende M, Di Sante G, Romano Spica V (2023) The S100B Protein: A Multifaceted Pathogenic Factor More Than a Biomarker. Int J Mol Sci. 24:9605. https://doi.org/10.3390/ijms24119605

38. Mitrofanova LB, Gorshkov AN, Konovalov PV, Krylova JS (2018) Telocytes in the human sinoatrial node. J Cell Mol Med 22:521–532. https://doi.org/10.1111/jcmm.13340

872 39. Mjaatvedt CH, Kern CB, Norris RA, Fairey S, Cave CL (2005) Normal distribution
873 of melanocytes in the mouse heart. Anat Rec A Discov Mol Cell Evol Biol. 285:748–57.
874 https://doi.org/10.1002/ar.a.20210
875 40. Moore BW (1965) A soluble protein characteristic of the nervous system. Biochem
876 Biophys Res Commun 19:739–744. https://doi.org/10.1016/0006-291x(65)90320-7
877 41. Morquette P, Verdier D, Kadala A et al (2015) An astrocyte-dependent mechanism
878 for neuronal rhythmogenesis. Nat Neurosci 18:844–854.
879 https://doi.org/10.1038/nn.4013
880 42. Nakamura T, Colbert MC, Robbins J (2006) Neural crest cells retain multipotential
881 characteristics in the developing valves and label the cardiac conduction system. Circ
882 Res. 98:1547–54. https://doi.org/10.1161/01.RES.0000227505.19472.69
883 43. Nayak MK, Du M, Vielman Quevedo R, Ly K, Bloom CR, Basch ML, Renauld J
884 (2026) Targeting the melanocytes of the inner ear: A comparison of different CreER
885 lines. Dev Biol. 530:224–233. https://doi.org/10.1016/j.ydbio.2025.12.009
886 44. Petersen J, Adameyko I (2017) Nerve-associated neural crest: peripheral glial cells
887 generate multiple fates in the body. Curr Opin Genet Dev. 45:10–14.
888 https://doi.org/10.1016/j.gde.2017.02.006
889 45. Quijada P, Trembley MA, Small EM (2020) The Role of the Epicardium During
890 Heart Development and Repair. Circulation Research 126:377–394.
891 https://doi.org/10.1161/CIRCRESAHA.119.315857
892 46. Rizvi TA, Huang Y, Sidani A, Atit R, Largaespada DA, Boissy RE, Ratner N (2002)
893 A novel cytokine pathway suppresses glial cell melanogenesis after injury to adult

894 nerve. J Neurosci. 22:9831–40. https://doi.org/10.1523/JNEUROSCI.22-22-
895 09831.2002
896 47. Saleh A, Smith DR, Tessler L et al (2013) Receptor for advanced glycation end-
897 products (RAGE) activates divergent signaling pathways to augment neurite outgrowth
898 of adult sensory neurons. Exp Neurol 249:149–159.
899 https://doi.org/10.1016/j.expneurol.2013.08.018
900 48. Scherschel K, Hedenus K, Jungen C, Lemoine MD, Rübsamen N, Veldkamp MW,
901 Klatt N, Lindner D, Westermann D, Casini S, Kuklik P, Eickholt C, Klöcker N, Shivkumar
902 K, Christ T, Zeller T, Willems S, Meyer C (2019) Cardiac glial cells release neurotrophic
903 S100B upon catheter-based treatment of atrial fibrillation. Sci Transl Med.
904 11:eaav7770. https://doi.org/10.1126/scitranslmed.aav7770
905 49. Smith-Thomas LC, Fawcett JW (1989) Expression of Schwann cell markers by
906 mammalian neural crest cells in vitro. Development. 105:251–62.
907 https://doi.org/10.1242/dev.105.2.251
908 50. Soldatov R, Kaucka M, Kastriti ME, Petersen J, Chontorotzea T, Englmaier L et al
909 (2019) Spatiotemporal structure of cell fate decisions in murine neural crest. Science
910 364:eaas9536. https://doi.org/10.1126/science.aas9536
911 51. Sun YH, Kao HKJ, Thai PN, Smithers R, Chang CW, Pretto D, Yechikov S,
912 Oppenheimer S, Bedolla A, Chalker BA, Ghobashy R, Nolta JA, Chan JW,
913 Chiamvimonvat N, Lieu DK (2023) The sinoatrial node extracellular matrix promotes
914 pacemaker phenotype and protects automaticity in engineered heart tissues from
915 cyclic strain. Cell Rep. 42:113505. https://doi.org/10.1016/j.celrep.2023.113505

52. Tomita Y, Matsumura K, Wakamatsu Y, Matsuzaki Y, Shibuya I, Kawaguchi H et al (2005) Cardiac neural crest cells contribute to the dormant multipotent stem cell in the mammalian heart. J Cell Biol.170:1135-46. https://doi.org/10.1083/jcb.200504061

53. Van Raamsdonk CD, Deo M (2013) Links between Schwann cells and melanocytes in development and disease. Pigment Cell Melanoma Res. 26:634–45. https://doi.org/10.1111/pcmr.12134

54. Villarreal A, Aviles Reyes RX, Angelo MF et al (2011) S100B alters neuronal survival and dendrite extension via RAGE-mediated NF-κB signaling. J Neurochem 117:321–332. https://doi.org/10.1111/j.1471-4159.2011.07207.x

55. Wang ZH, Walter GF, Gerhard L (1996) The expression of nerve growth factor receptor on Schwann cells and the effect of these cells on the regeneration of axons in traumatically injured human spinal cord. Acta Neuropathol. 91:180–4. https://doi.org/10.1007/s004010050411

56. Yajima I, Larue L (2008) The location of heart melanocytes is specified and the level of pigmentation in the heart may correlate with coat color. Pigment Cell Melanoma Res. 21:471–6. https://doi.org/10.1111/j.1755-148X.2008.00483.x

57. Zhou Y, Zha Y, Yang Y, Ma T, Li H, Liang J (2023) S100 proteins in cardiovascular diseases. Mol Med. 29:68. https://doi.org/10.1186/s10020-023-00662-1

58. Zhu Y, Li X, Janairo RRR, Kwong G, Tsou AD, Chu JS, Wang A, Yu J, Wang D, Li S (2019) Matrix stiffness modulates the differentiation of neural crest stem cells in vivo. J Cell Physiol. 234:7569–7578. https://doi.org/10.1002/jcp.27518

FIGURE LEGENDS

Figure 1. Panoramic 3D reconstruction of the HCN4$^+$ pacemaker meshwork and spatial morphotypes of S100B$^+$ interstitial cell distribution in the murine SAN.

Tiled panoramic reconstructions of the SAN showing three morphotypes of S100B$^+$-immunoreactive interstitial cell organization (cyan) relative to the HCN4$^+$ pacemaker meshwork (red). **Panel A (Patchy morphotype):** S100B$^+$ cells form discrete clusters (yellow ROI) separated by S100B$^-$ cell-free gaps (white ROI). Dispersed solitary cells can also be detected (red ROI). **Panel B (Contiguous morphotype):** S100B$^+$ clusters (yellow ROI) merge into a nearly continuous distribution, alternating with regions of lower density (red ROI) but lacking S100B$^+$-free gaps. **Panel C (Solitary morphotype):** S100B$^+$ cells are scattered as solitary interstitial cells without recognizable clusters. **Panels A1, B1, C1:** Composite overlays of HCN4 (red) and S100B (cyan) immunoreactivity highlight the interwoven relationship of pacemaker and interstitial cells. **Panels A2, B2, C2:** S100B immunoreactivity alone, emphasizing cluster formation (A, B) or dispersed distribution (C). Yellow ROIs = representative clusters; red ROIs = regions with S100B$^+$ interstitial cells but no clusters; white ROIs = S100B$^+$ interstitial cell-free gaps. **Panels A3, B3, C3:** Transmitted light images of the same regions showing tissue pigmentation patterns: patchy in the patchy morphotype (yellow ROI pigment clusters), broadly contiguous in the contiguous morphotype (red ROI), and largely absent in the solitary morphotype. Green ROIs in Panels C2 and C3 mark the HCN4$^+$ meshwork corresponding to Panel C1.

Figure 2. Quantitative analysis of S100B$^+$ fluorescence intensity distinguishes three SAN morphotypes.

Panel A: Averaged fluorescence intensity profiles of S100B$^+$ labeling along the SVC–IVC axis, showing solitary (green), patchy (black), and contiguous (red) morphotypes. Data represent means from four independent datasets. **Panel B:** Quantification of area under the curve (AUC) from the same datasets confirmed significant differences among all three morphotypes. One-way ANOVA revealed a highly significant overall effect ($F(2,57) = 4440.63$, $P < 0.0001$). Tukey's HSD post hoc test showed that the patchy morphotype was modestly but significantly higher than the solitary morphotype ($P = 0.0001$), whereas the contiguous morphotype was substantially higher than both ($P < 0.0001$ for all pairwise comparisons). **Panel C:** Orthogonal 3D views of Z-stacks (320 µm × 150 µm × 70 µm) show XY (green frame) and XZ planes (yellow frame) illustrating endocardial–epicardial distribution of S100B$^+$ interstitial cells. Cells were either evenly distributed across the thickness of the SAN (Panel C1) or polarized toward the endocardial (Panel C2) or epicardial side (Panel C3).

Figure 3. Clusters of dendritic-dominant and amoeboid S100B$^+$ interstitial cells with associated tissue pigment in the SAN.

Panels A and B: Clusters of S100B$^+$ interstitial cells (cyan) embedded within the HCN4$^+$ pacemaker meshwork (red), overlapped with transmitted light images to illustrate colocalization of S100B$^+$ immunoreactivity with tissue pigment. Yellow arrows indicate pigmented dendritic interstitial cells (black pigment in Panel A, dark gray in Panel B); red arrows mark pigmented amoeboid interstitial cells. Notably, in the dendritic cell (Panel A,

yellow arrow) and amoeboid cell (Panel B, red arrow), only nuclei are visible in the fluorescent channel due to dense pigmentation. **Panel C:** Cluster of S100B$^+$ interstitial cells located in a region with barely detectable pigmentation. **Panels A1, B1, C1:** Overlays of HCN4 (red) and S100B (cyan) immunoreactivity. **Panels A2, B2, C2:** S100B$^+$ interstitial cells (cyan) alone. **Panels A3, B3, C3:** Transmitted light images co-localized with S100B$^+$ cells. **Panels A4, B4, C4:** Transmitted light images of SAN tissue highlighting pigmented melanocyte-like cells.

Figure 4. Clusters of dendritic and amoeboid-dominant S100B$^+$ interstitial cells with associated tissue pigment in the SAN.

Panels A and B illustrate clusters of S100B$^+$ interstitial cells (cyan) embedded within the HCN4$^+$ pacemaker meshwork (red), overlapped with transmitted light images to illustrate colocalization of S100B$^+$ immunoreactivity with tissue pigment. Yellow arrows indicate pigmented amoeboid interstitial cells; white arrows mark unpigmented amoeboid interstitial cells. Notably, in the pigmented amoeboid cell, only nuclei are visible in the fluorescent channel due to dense pigmentation. **Panel C:** Cluster of S100B$^+$ interstitial cells located in a region with barely detectable pigmentation. **Panels A1, B1, C1:** Overlays of HCN4 (red) and S100B (cyan) immunoreactivity. **Panels A2, B2, C2:** S100B$^+$ interstitial cells (cyan) alone. **Panels A3, B3, C3:** Transmitted light images co-localized with S100B$^+$ cells. **Panels A4, B4, C4:** Transmitted light images of SAN tissue highlighting pigmented melanocyte-like cells.

Figure 5. Pigmented vesicles in S100B$^+$ interstitial cells within the SAN.

S100B$^+$ interstitial cells (cyan) embedded in the HCN4$^+$ pacemaker meshwork (red) contain intracellular vesicles ranging from 200–500 nm in size and varying in pigment density from light gray to pitch black (red arrows), often coexisting within the same cellular branches. Despite dense pigmentation, S100B$^+$ fluorescence remained visible in perinuclear regions and distal branches. **Panel 1A:** Irregular plexus of intertwined S100B$^+$ interstitial cells (cyan), merged with transmitted light, with three ROIs indicated (yellow boxes). **Panel 1B:** Transmitted light image of the same field, with nuclei labeled by DAPI. **Panel 2A:** ROI2 showing S100B$^+$ interstitial cells (cyan) embedded within the HCN4$^+$ pacemaker cell meshwork (red). **Panel 2B:** Corresponding transmitted light image of ROI2 with DAPI-stained nuclei. **Panel 3A:** Transmitted light image of ROI3 with DAPI-stained nuclei. **Panel 3B:** ROI3 showing S100B$^+$ interstitial cells (cyan) merged with transmitted light. **Panel 4A:** ROI4 showing S100B$^+$ interstitial cells (cyan) merged with transmitted light. **Panel 4B:** Corresponding transmitted light image of ROI4 with DAPI-stained nuclei.

Figure 6. Ultrastructural overview of SAN pigmented areas obtained by TEM microscopy.

Ultrastructural analysis revealed melanocyte-like interstitial cells with two morphometrically distinct phenotypes: dendritic and amoeboid. **Panel A:** Toluidine blue–stained semithin section of a longitudinally cut SAN illustrating pigmented tissue areas and cellular heterogeneity. **Panels B–E:** Colored mosaic TEM images of pigmented interstitial cells, with dendritic cells pseudocolored in blue and amoeboid cells in red. Dendritic cells contain elongated cytoplasmic processes (podoms) filled with

melanosome-like vesicles, highlighted by yellow stars. The green arrow indicates the main cell body of a dendritic cell. Pigmented vesicles appear as optically dark, electron-dense structures of variable size (200–500 nm) and density, ranging from light gray to pitch black, and are scattered throughout the cytoplasm of both dendritic and amoeboid cells. A greater diversity of electron-dense pigmented vesicles is observed in amoeboid (red) cells, reflecting their larger cell volume and the higher number of vesicles captured per unit volume within a single visual plane. These ultrastructural features correspond to the intracellular pigmented vesicles detected by confocal microscopy in S100B^{+} interstitial cells (Figures 3–5), linking pigment distribution to cellular morphotypes within the SAN.

Figure 7. Dendritic cell intercellular communication.

TEM images illustrate ultrastructural features of pigmented dendritic interstitial cells within the SAN. **Panel A:** Detail of a densely pigmented dendritic process showing heterogeneous vesicles at different maturation stages, ranging from lightly pigmented to highly electron-dense melanosome-like structures. Vesicles varied in size (100–500 nm). **Panels B and C:** Tiled TEM mosaics of large longitudinal cross-sections through dendritic cell bodies and extensions. Yellow stars mark pigment clusters, while red arrows indicate loose synaptic-like contacts with pacemaker cell membranes, suggesting potential signaling interfaces. **Panel D:** Detail of a close apposition between a dendritic telopode and a peripheral nerve, indicated by the green arrow, consistent with a specialized functional unit of pigmented–neuro–pacemaker cell interactions. Vesicles display substantial variability in size, packing density per volume, and maturation state, consistent with active pigment synthesis, turnover, and trafficking.

Figure 8. Morphology and maturation stages of pigmented intracellular vesicles in SAN interstitial cells.

TEM images of highly pigmented SAN regions. **Panel A:** Amoeboid interstitial cell with cytoplasm densely filled by heterogeneous pigmented vesicles ranging from 100 to 500 nm, varying in size, packing density, and maturation state. **Panels B–F:** Sequential ultrastructural stages of vesicle maturation (I–IV). Stage I vesicles appear as lightly structured compartments with minimal pigmentation; Stage II vesicles display fibrillar substructure with initial pigment deposition; Stage III vesicles show progressive darkening and increased size with further pigment accumulation; Stage IV vesicles are fully electron-dense, representing mature granules. **Panel D:** Red numbers (1–5) mark a continuum of vesicles transitioning from Stage II to Stage III, illustrating progressive pigment deposition. These images show that SAN pigment resides within discrete vesicular compartments undergoing stepwise structural and pigmentary changes.

Figure 9. Amoeboid pigmented cells in the SAN.

TEM images of pigmented interstitial cells illustrate that intracellular pigmented vesicles in SAN melanocytes can be produced either as single units or as multiple vesicles enclosed within a common limiting membrane, forming complex multivesicular bodies with heterogeneous cargo. **Panel A:** Mosaic image of a large amoeboid pigmented cell fragment, with a yellow star marking the release of pigmented vesicle clusters. **Panel B:** Extracellular pigmented vesicles in the interstitial space, displaying variable electron density and heterogeneous surface coats, consistent with differences in cargo and suggesting distinct trafficking pathways toward different recipient cells.

Figure 10. Proliferative activity within the SAN assessed by EdU labeling.

EdU-positive nuclei (yellow) were scattered randomly throughout the $HCN4^+$ pacemaker cell meshwork (red), extending from the SAN head to the tail (**Panels A–C**, images taken at the corresponding regions). Colocalization of EdU with DAPI signals confirmed nuclear identity. All EdU-labeled nuclei localized to interstitial spaces within the meshwork, with none detected inside $HCN4^+$ pacemaker cells. **Panel D:** Example of semi-automatic nuclear detection within a 600 × 600 µm area, used to obtain total nuclear counts and calculate EdU labeling indices across SAN regions. The proportion of EdU-labeled to total nuclei was low and consistent, averaging 6.7% in the head, 5.7% in the body, and 6.1% in the tail. Statistical analyses revealed no significant regional differences in labeling indices (one-way ANOVA, $F = 0.16$, $P = 0.86$; pairwise *t*-tests, all $P > 0.55$) or in absolute EdU^+ nuclei counts (one-way ANOVA, $F(2,17) = 1.18$, $P = 0.33$; head: 32.7 ± 4.8, $n = 7$; body: 24.0 ± 5.0, $n = 6$; tail: 23.0 ± 5.1, $n = 7$).

Figure 11. Spatial distribution of EdU^+ nuclei along the endo–epicardial axis of the SAN.

Z-stack images were post-processed with orthogonal sectioning to generate 3D reconstructions of EdU-labeled nuclei. A distinct layered arrangement, such as the germinative zones of basal epidermis or intestinal crypts, was not observed. Instead, three distribution patterns were identified: nuclei polarized toward the epicardial side (**Panel A**), nuclei polarized toward the endocardial side (**Panel B**), and nuclei distributed

homogeneously across the axis (**Panel C**). Examples shown are from the SAN head, body, and tail; however, all three patterns were observed in each region.

Figure 12. EdU$^+$ nuclei within S100B$^+$ interstitial cell nests of the SAN.

Orthogonal sectioning of 3D reconstructions demonstrated 3D-colocalization of EdU$^+$ nuclei with S100B$^+$ interstitial cells (cyan) embedded in the HCN4$^+$ pacemaker cell meshwork (red). **Panels A and B:** EdU$^+$ nuclei (yellow) colocalized within compact nests of S100B$^+$ interstitial cells. **Panels C–F:** Examples of nests with two or more EdU$^+$ nuclei, with small belt of perinuclear S100B$^+$-immunoreactive cytoplasm. **Panel G:** Example of two closely apposed S100B$^+$ interstitial cells containing EdU$^+$ nuclei that had begun to separate, connected by cytoplasmic bridges.

Figure 13. EdU$^+$ nuclei within pigmented melanocyte-like nests of the SAN.

Panel A: Confocal image (300 × 300 µm) of the HCN4$^+$ pacemaker cell meshwork (red) containing S100B$^+$ immunoreactive nests (cyan) in a pigmented SAN region. EdU$^+$ nuclei (yellow) are localized within compact nests of heavily pigmented interstitial cells. Black regions represent pigmented tissue where melanin absorbs emitted fluorescence, producing signal voids. **Panels B, C:** Pigmented nests containing EdU$^+$ nuclei (white arrows). In these nests, dense pigmentation obscures cellular membranes and cytoplasmic detail, restricting visualization primarily to nuclei. **Panel D:** Higher-magnification view of pigmented melanocyte-like SAN cells, in which pigmented vesicles surround EdU$^+$ nuclei. Increased cytoplasmic volume and the emergence of filopodia/pseudopodia are evident. **Panels E–G:** Solitary EdU$^+$ pigmented interstitial cells

displaying amoeboid morphology with pseudopodia, consistent with migratory phenotypes. **Panel H:** Solitary amoeboid EdU^+ nuclei (white arrow) and dendritic melanocyte-like cells (green arrows) detected hundreds of micrometers from the EdU^+ nests, indicating dispersal of pigmented interstitial cells within the $HCN4^+$ meshwork.

Figure 14. Dispersal of EdU^+ $S100B^+$ interstitial cells from nests into the SAN meshwork.

Panels A, B: Adjacent EdU^+ $S100B^+$ interstitial cells with distinct cellular boundaries, consistent with cells that may have separated from a common nest. **Panels C, D:** Solitary EdU^+ $S100B^+$ interstitial cells exhibiting amoeboid morphology with pseudopodia, indicative of migratory behavior. These cells were detected hundreds of micrometers from EdU^+ nests within the $HCN4^+$ pacemaker cell meshwork, suggesting that proliferating $S100B^+$ interstitial cells can disperse and migrate prior to adopting differentiated morphologies. **Panel E:** $S100B^+$ immunoreactive interstitial cells forming an irregular dendritic plexus (cyan), within which some cells contain EdU^+ nuclei (yellow arrow) and intertwined with $HCN4^+$-immunoreactive (red color) meshwork. An $S100B^+/EdU^+$ nest is located in the lower right portion of the image (white arrow).

Supplemental Figure 1. Structural organization of $S100B^+$ interstitial cells and peripheral glial cells (PGCs) within the SAN.

Panel A: Confocal images show $S100B^+/GFAP^-$ interstitial cells and $S100B^+/GFAP^+$ peripheral glial cells (PGCs) embedded within the $HCN4^+$ pacemaker meshwork. Pink/orange arrows indicate amoeboid $S100B^+/GFAP^-$ interstitial cells; white arrows

indicate dendritic S100B$^+$/GFAP$^-$ interstitial cells; and yellow arrows mark S100B$^+$/GFAP$^+$ PGCs. Radiating branches of PGCs form an organized intercellular plexus, while a thick branching nerve fiber ensheathed by PGCs is indicated by a cyan arrow. **Panels B, C:** Higher magnification views showing dendritic (white arrows) and amoeboid (pink/orange arrows) S100B$^+$/GFAP$^-$ interstitial cells (cyan) interspersed among and closely apposed to HCN4$^+$ pacemaker cells (red). **(A1, B1, C1)** Merged images of HCN4 (red), S100B (cyan), and GFAP (green) immunoreactivity in the SAN. **(A2, B2, C2)** Overlays of S100B (cyan) and GFAP (green) channels highlighting the distinct spatial relationship between interstitial cells and PGCs. **(A3)** Detailed view of S100B (cyan) immunoreactivity illustrating the phenotypic and cytoarchitectural diversity of interstitial cells and PGCs.

Supplemental Figure 2. Developmental and age-related persistence of S100B$^+$ interstitial cells within the SAN pacemaker meshwork.

Panels A–C: Representative confocal images of the HCN4$^+$ pacemaker cell meshwork (red) with S100B$^+$ interstitial cells (cyan) at three life stages: **(A)** prenatal P12 embryo, when the heart was already formed and exhibited intrinsic myogenic pacemaker activity; **(B)** 6-month-old adult mouse; and **(C)** 28-month-old aged mouse. At all stages, S100B$^+$ interstitial cells remain consistently associated with the HCN4$^+$ network. The prenatal meshwork appears more uniform, whereas adult and aged SAN tissue display greater phenotypic heterogeneity, reflecting age-related remodeling of the pacemaker structure. Despite these changes, the continuous presence of S100B$^+$ interstitial cells—

from early embryonic assembly through advanced age—supports their foundational role in sustaining pacemaker architecture and function across the lifespan.

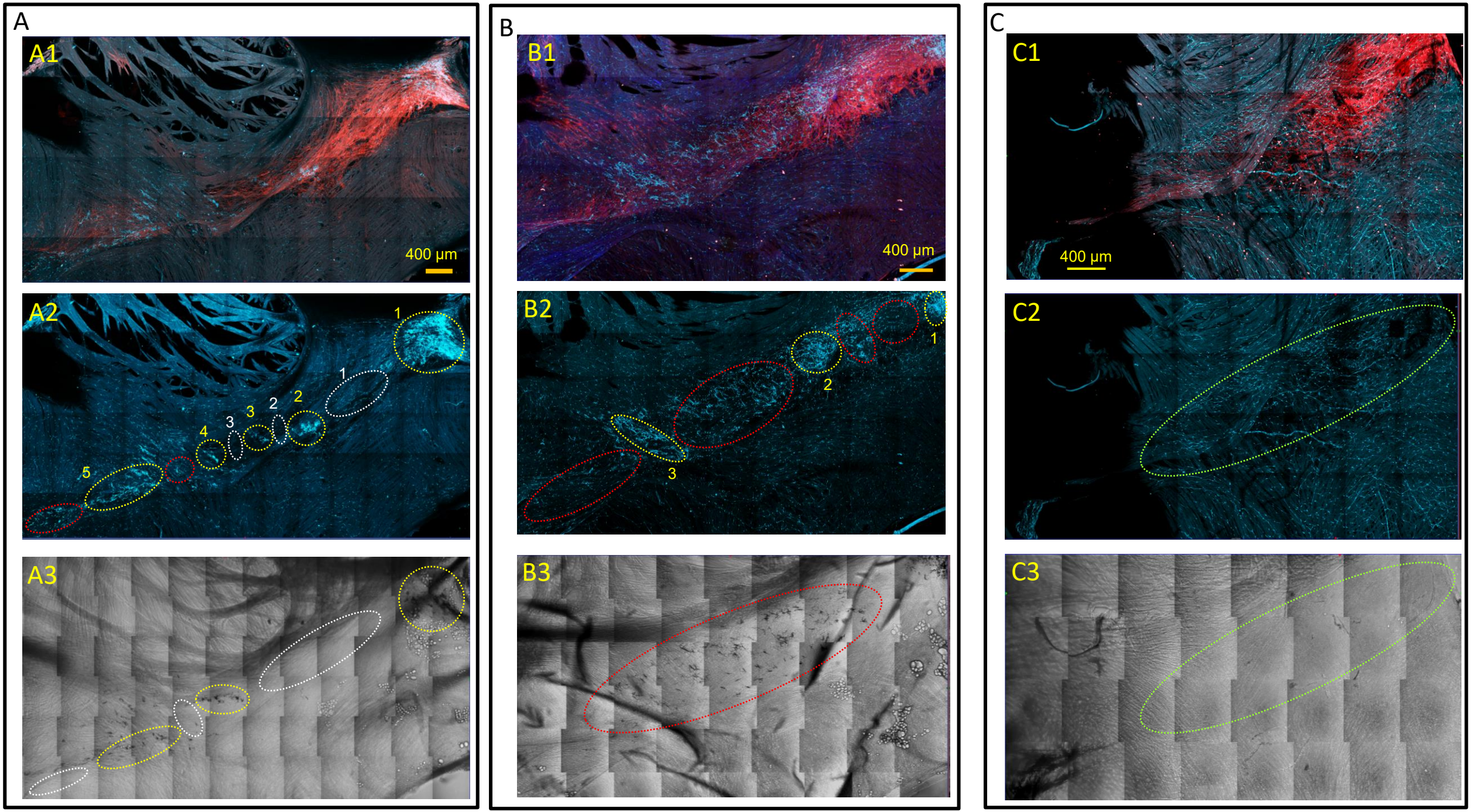

Fig.1

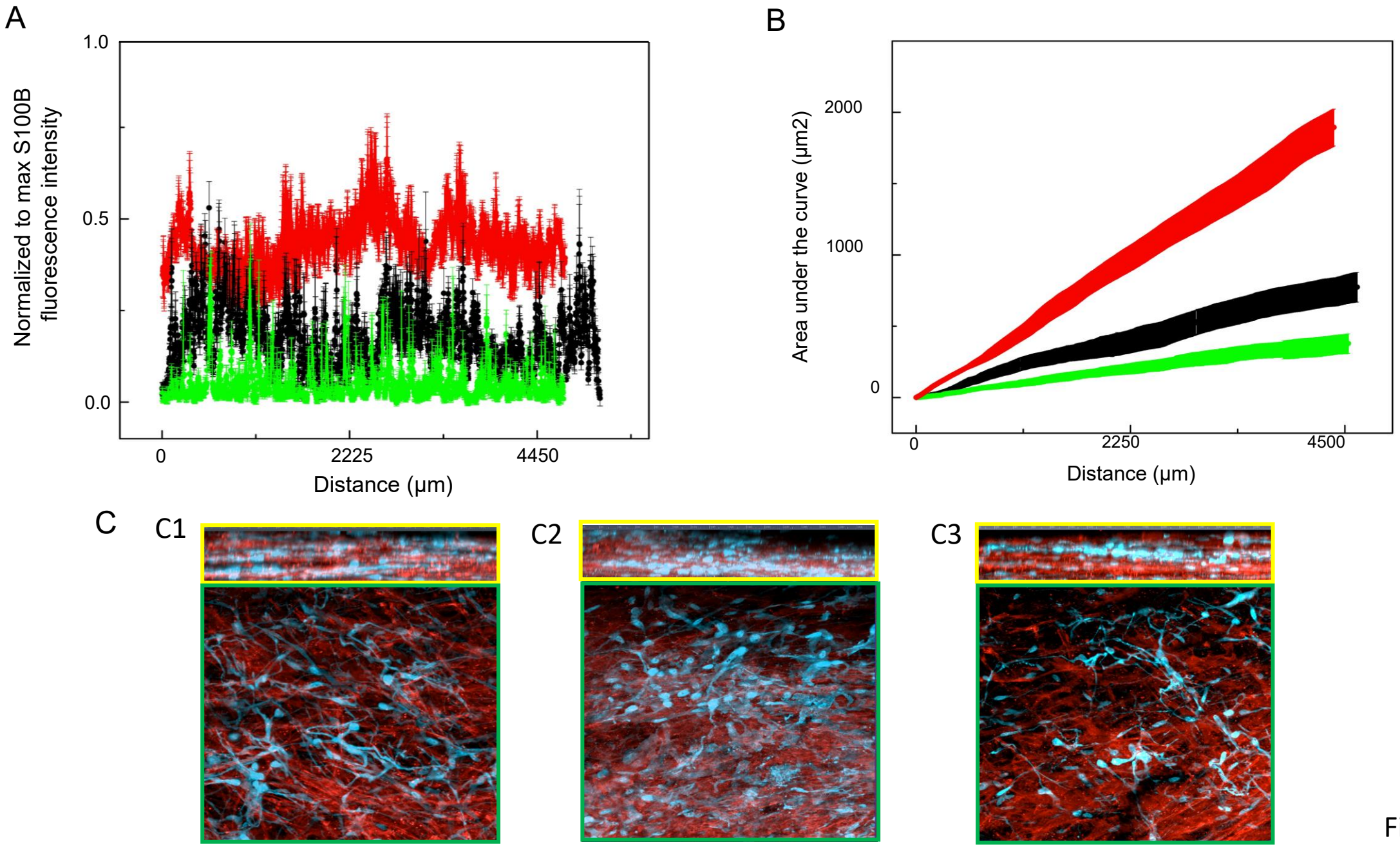
A
1.0
0.5
0.0
Normalized to max S100B fluorescence intensity
0
2225
4450
Distance (μm)
B
2000
1000
0
Area under the curve (μm2)
0
2250
4500
Distance (μm)
C
C1
C2
C3

Fig. 2

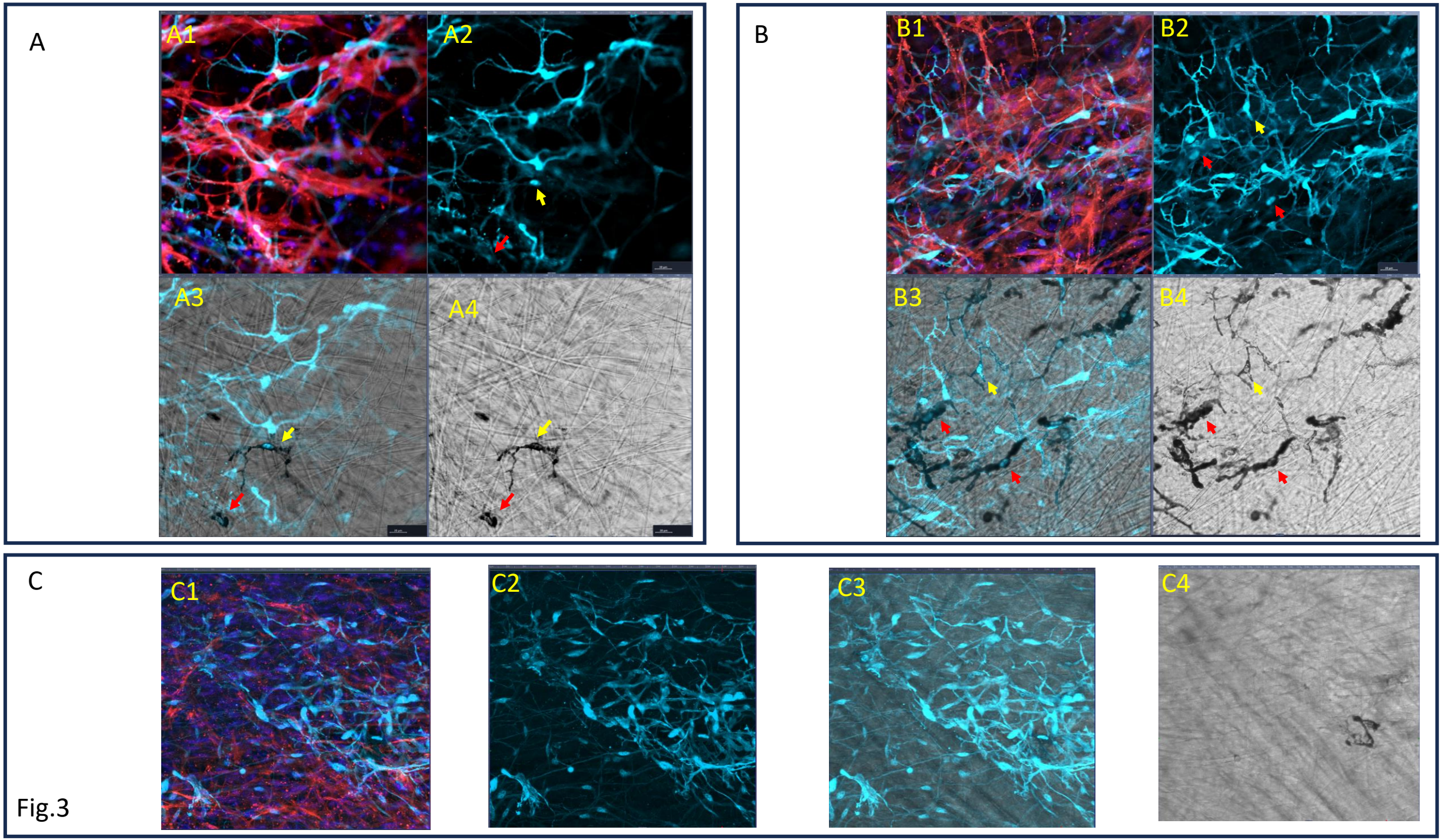

Fig.3

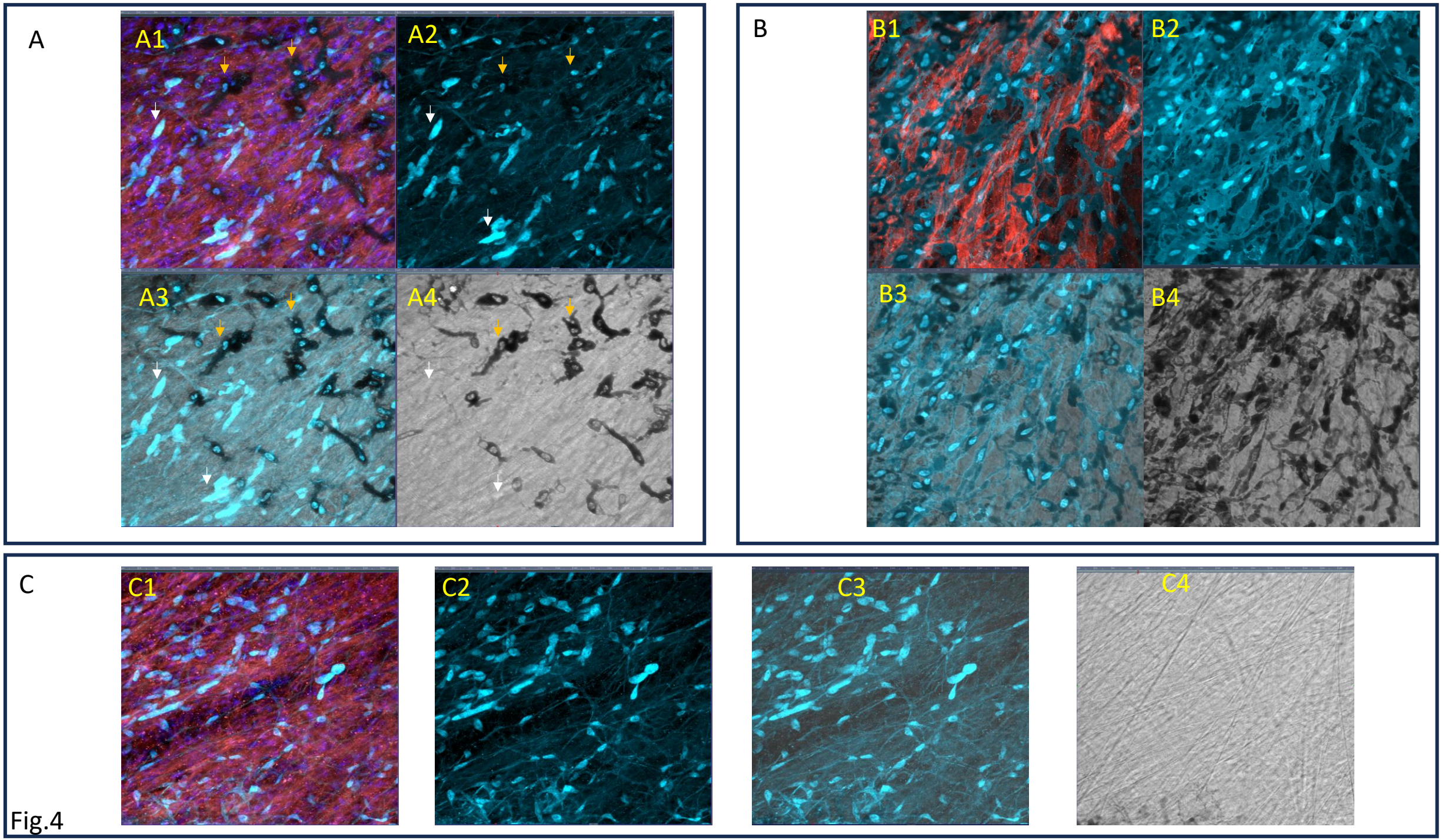

Fig.4

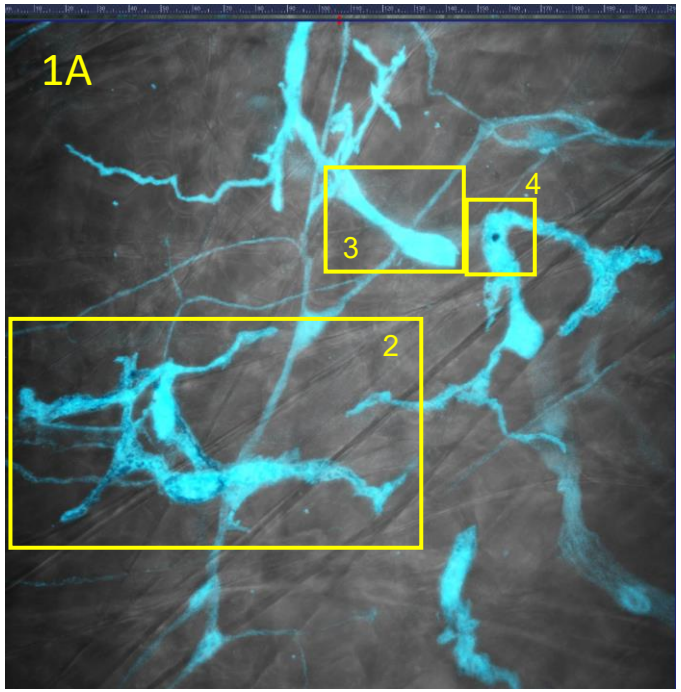

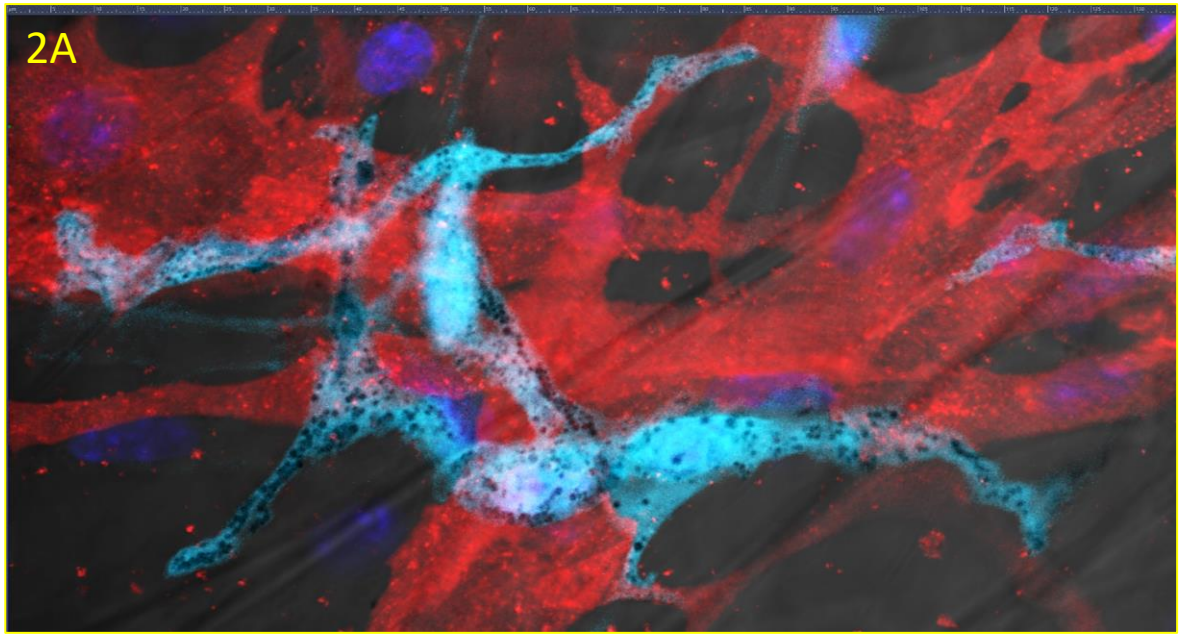

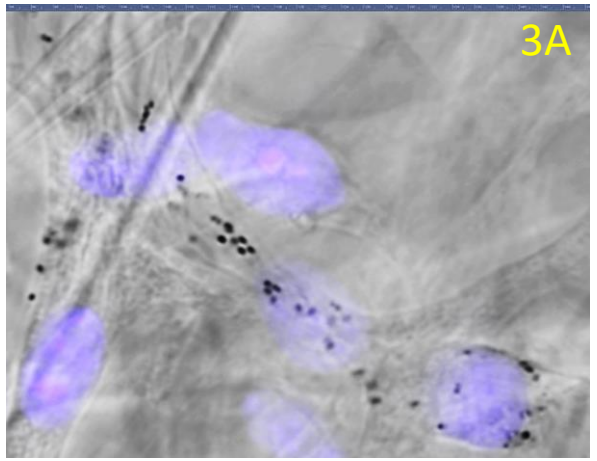

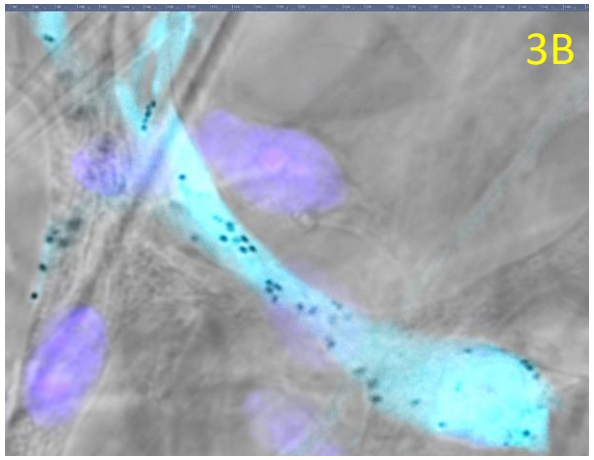

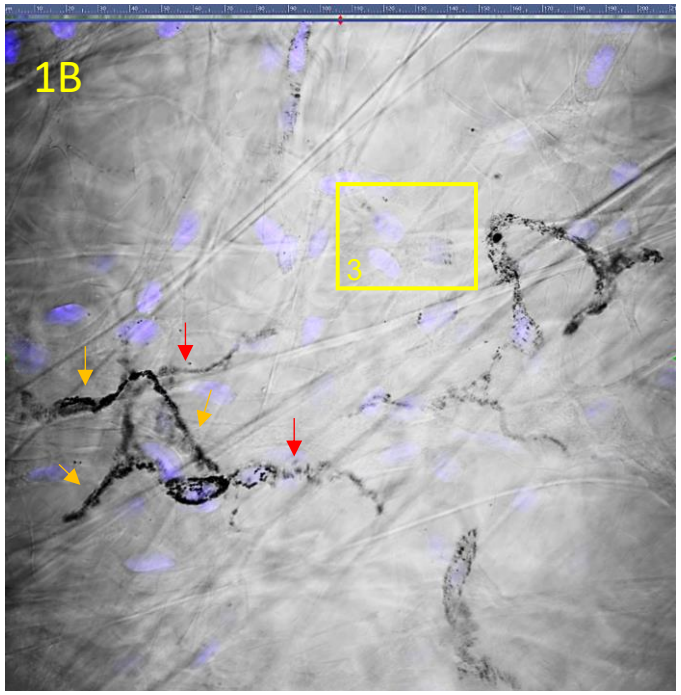

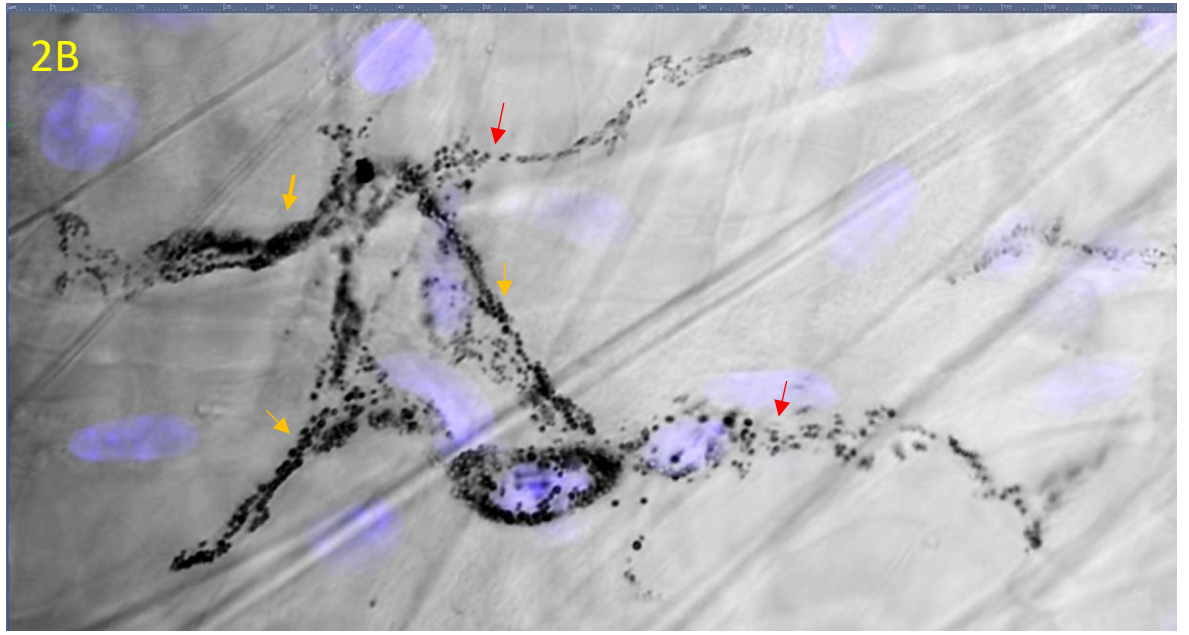

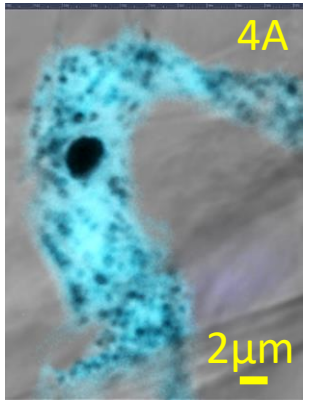

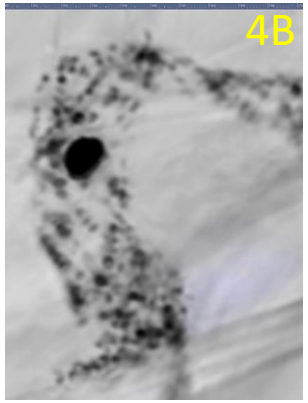

Fig.5

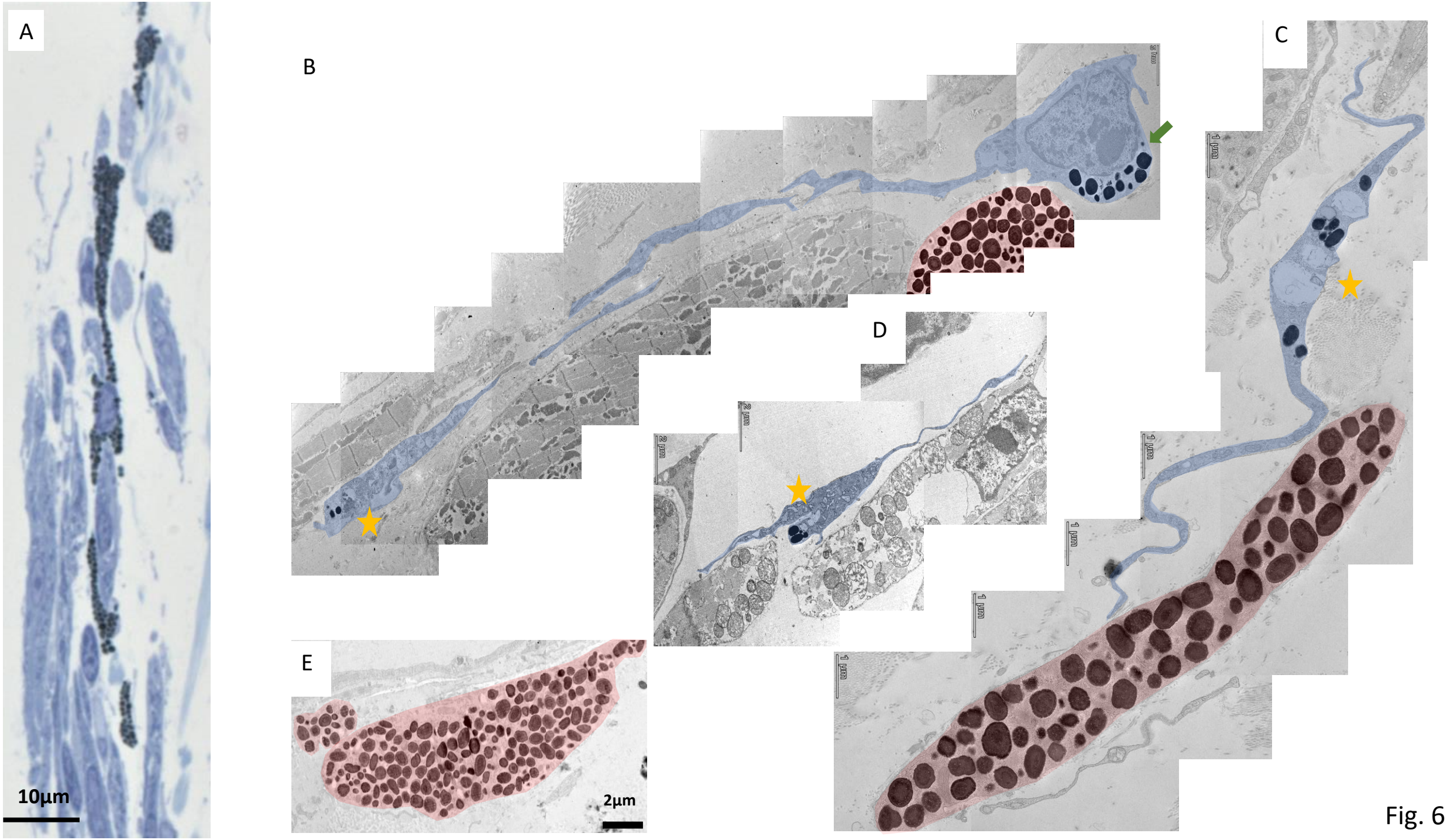

Fig. 6

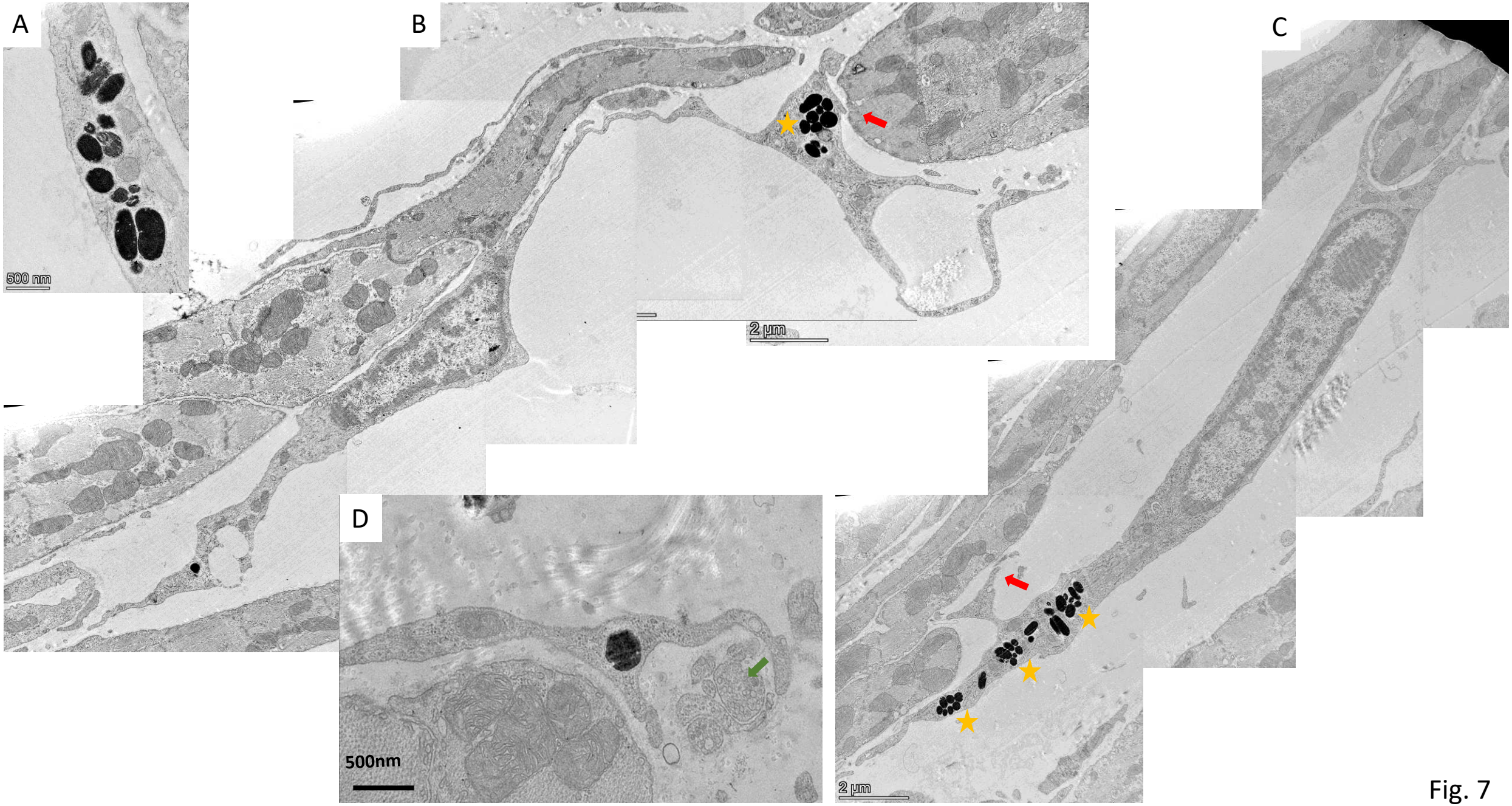

Fig. 7

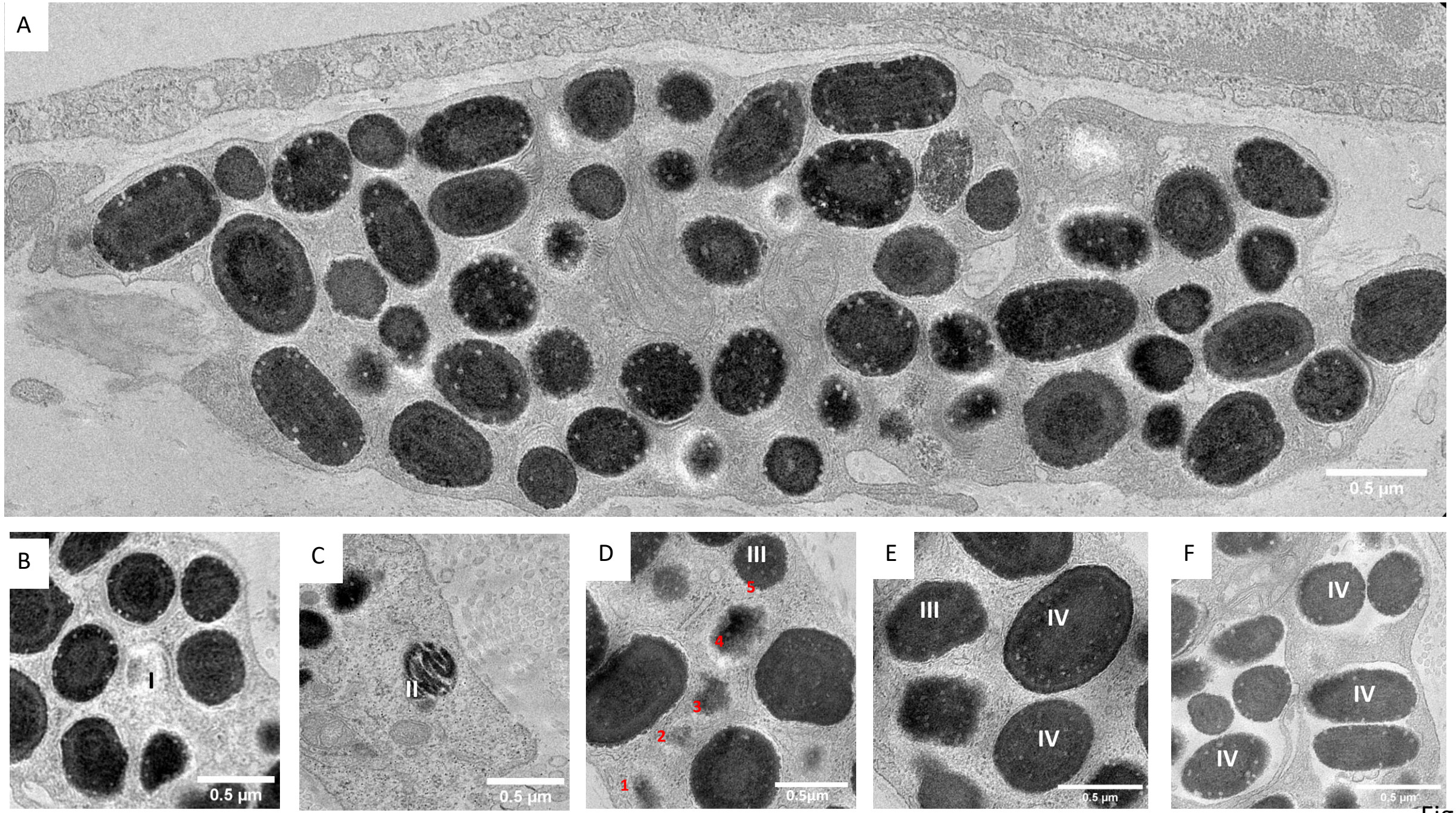
A
0.5 µm
B
I
0.5 µm
C
II
0.5 µm
D
III
5
4
3
2
1
0.5µm
E
III
IV
IV
0.5 µm
F
IV
IV
IV
0.5 µm

Fig. 8

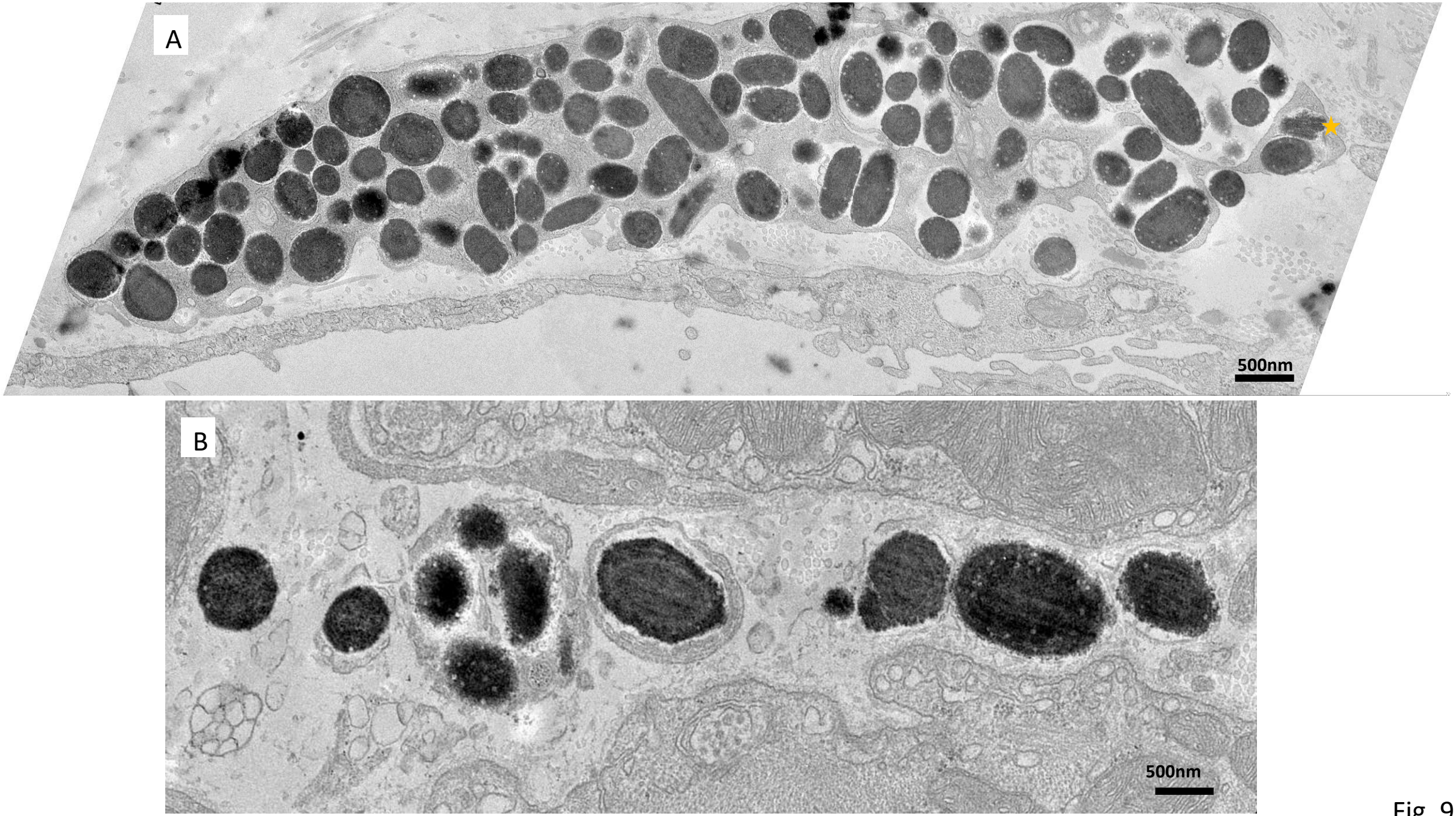

Fig. 9

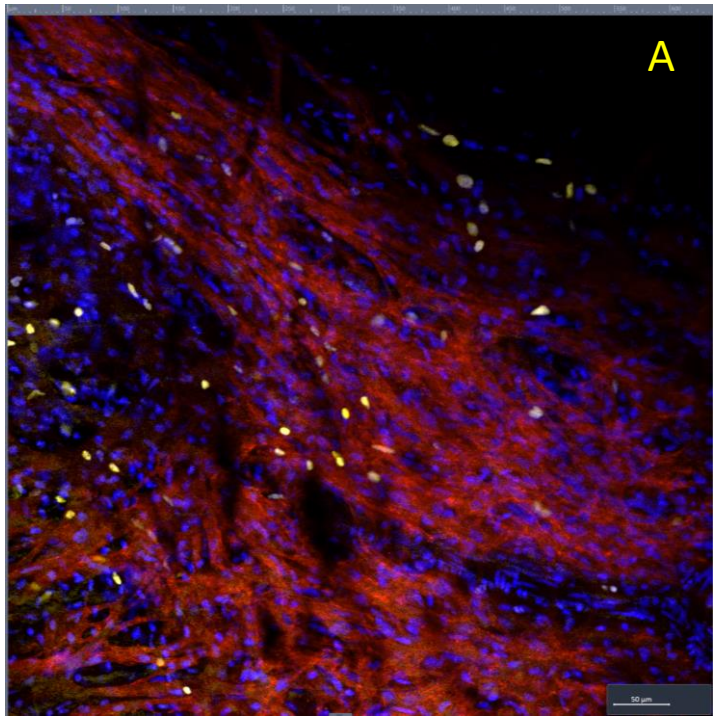
A

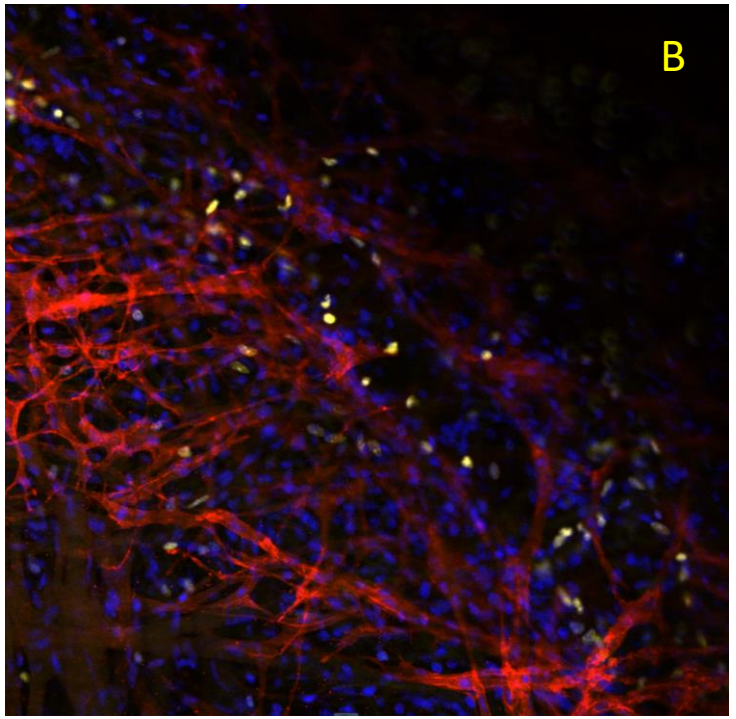
B

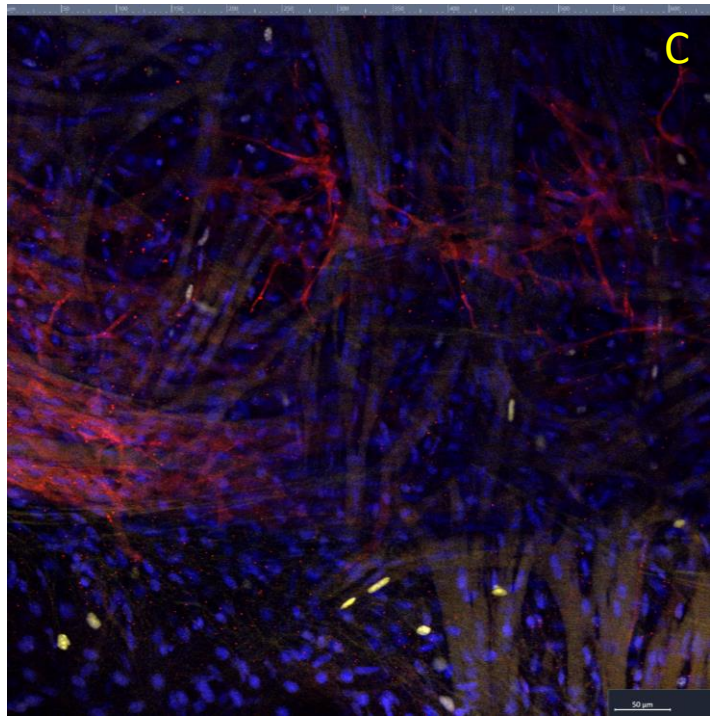
C

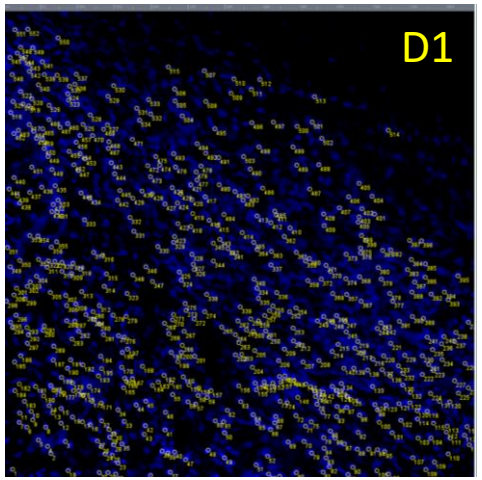
D1

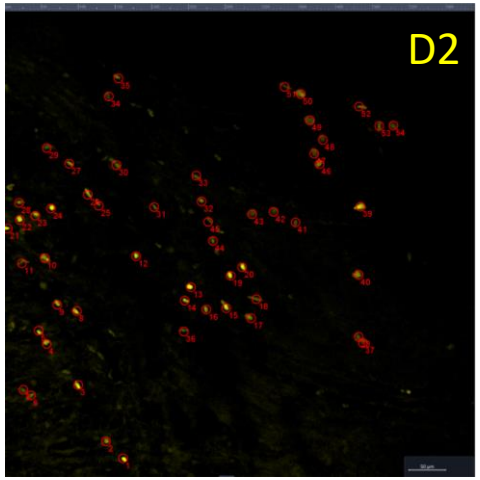
D2

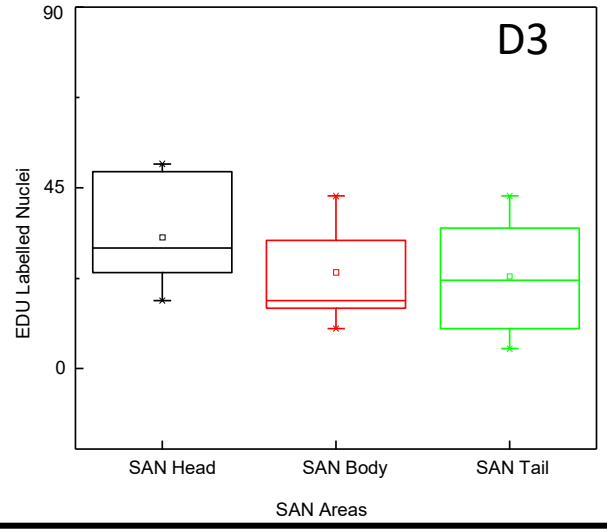
D3
90
45
0
EDU Labelled Nuclei
SAN Head
SAN Body
SAN Tail
SAN Areas

Fig.10

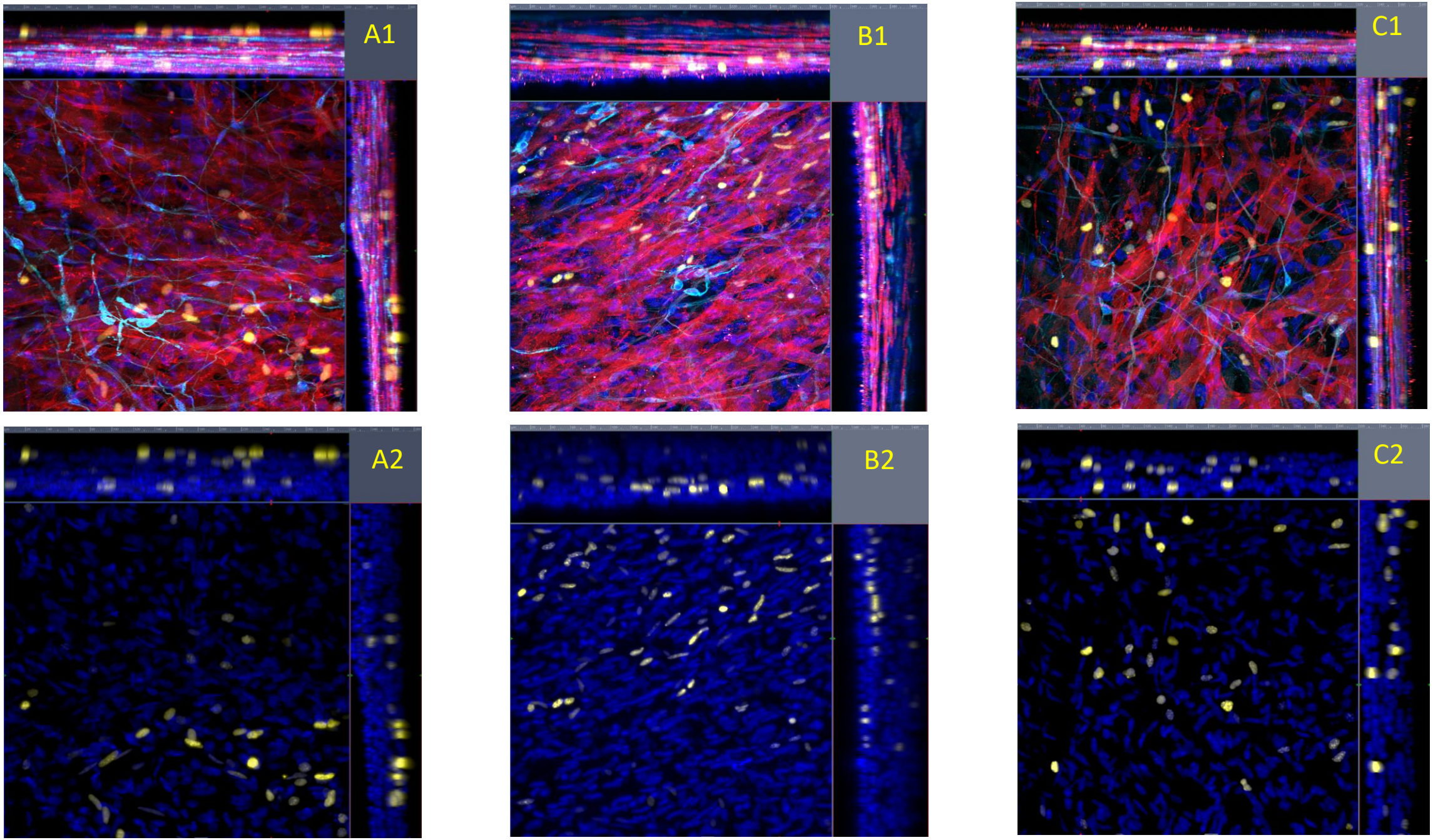

Fig.11

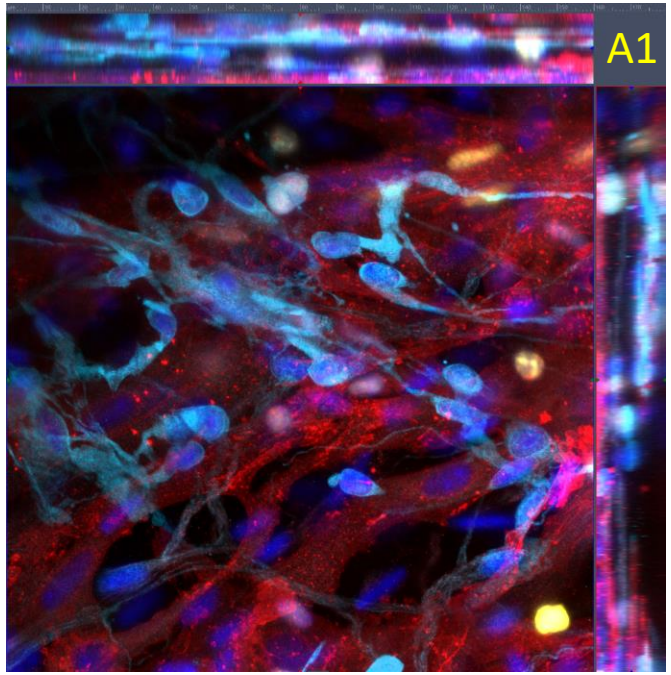

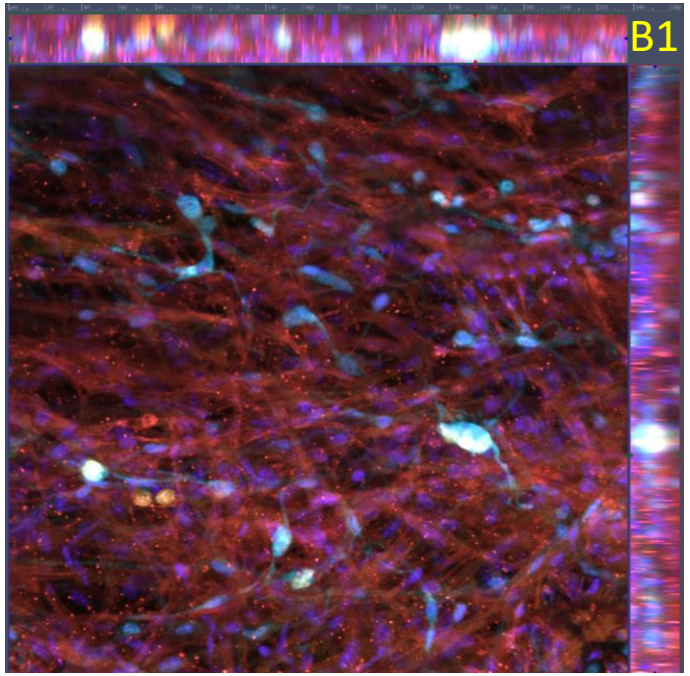

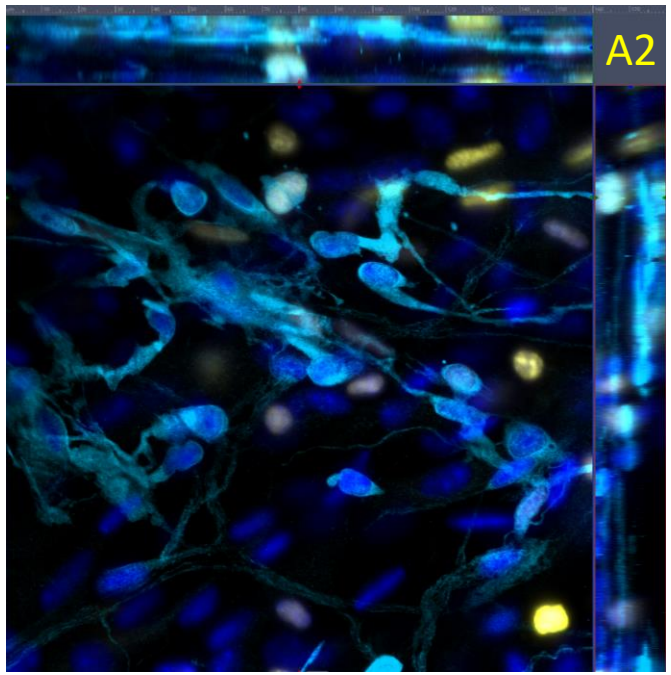

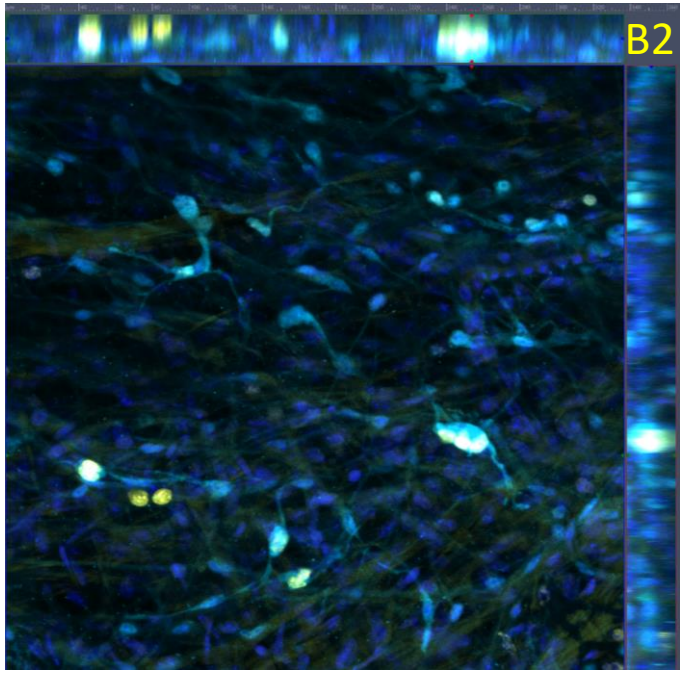

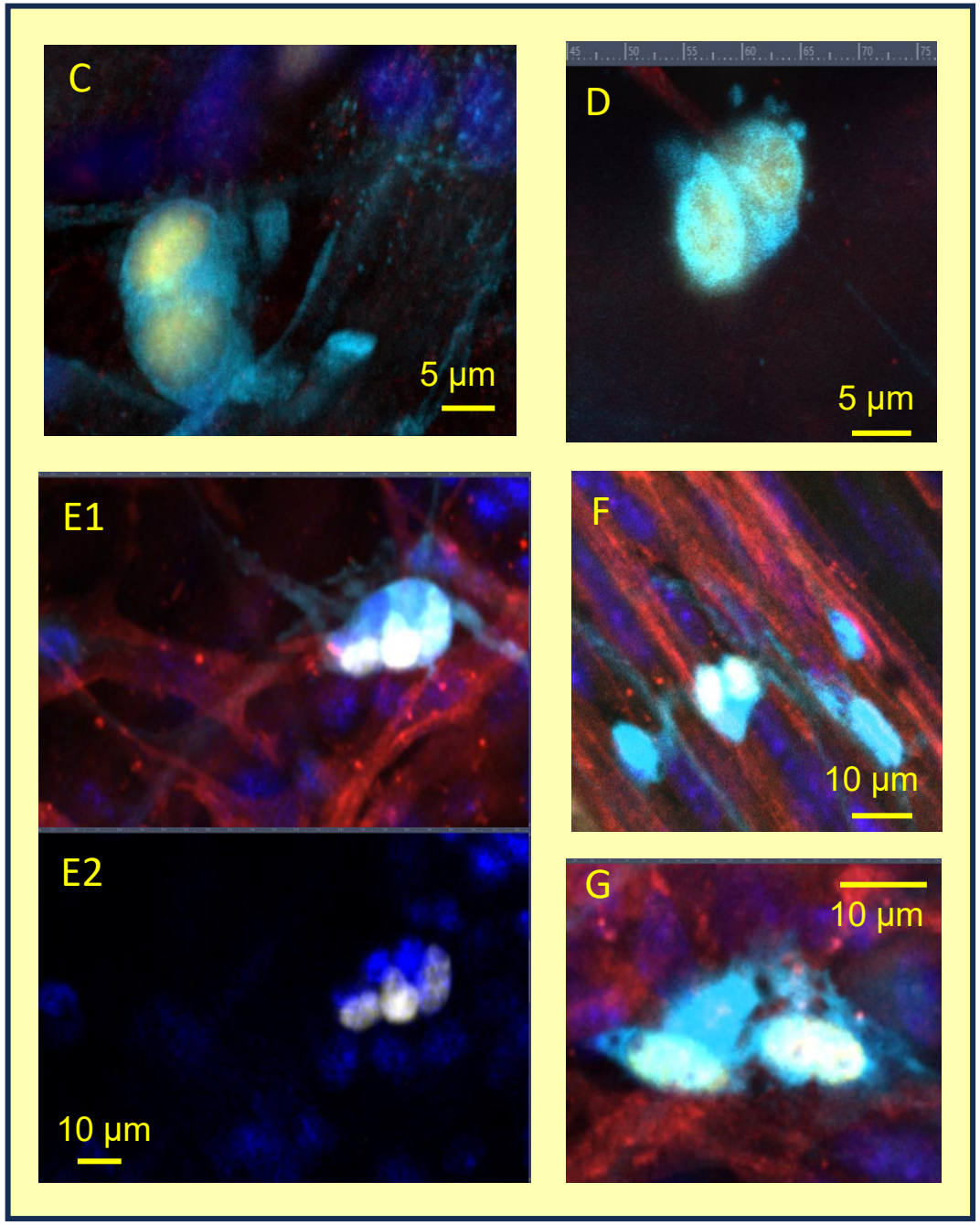

Fig.12

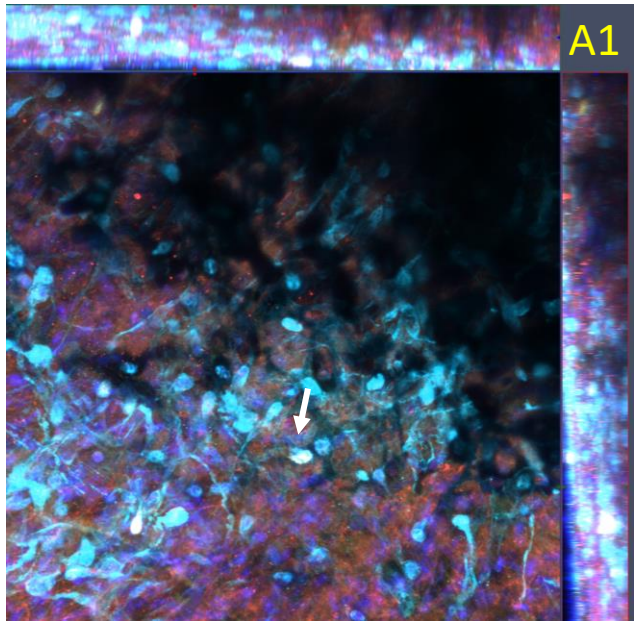

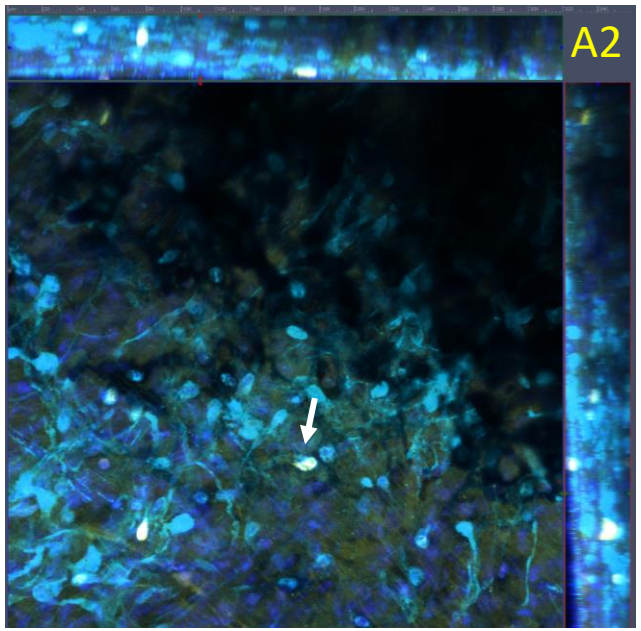

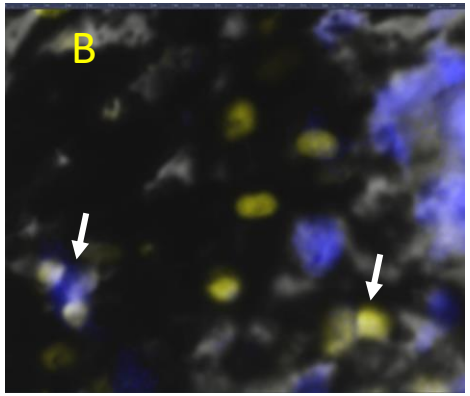

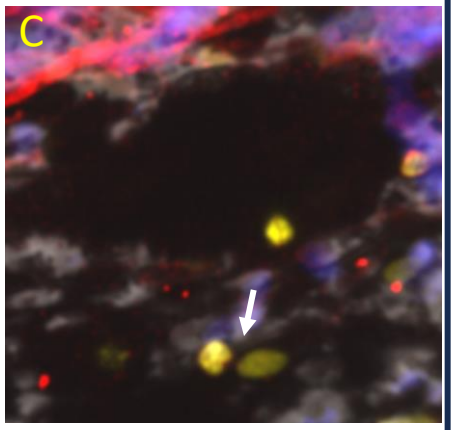

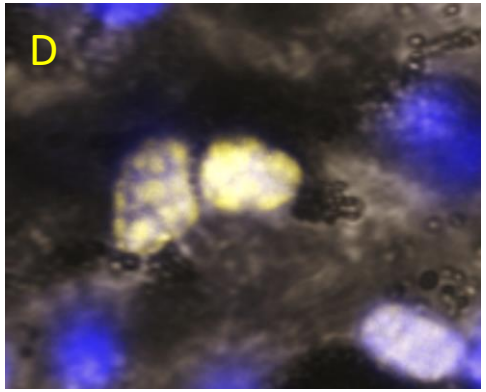

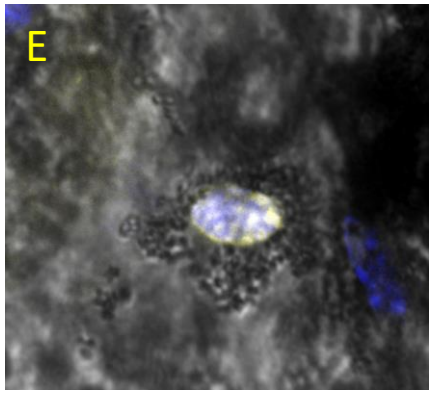

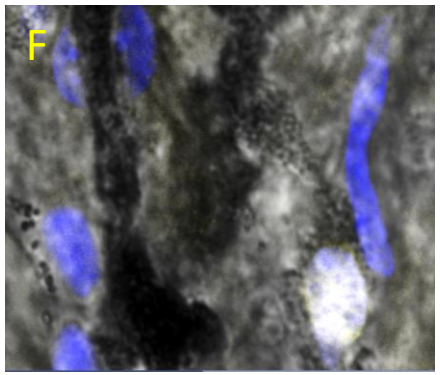

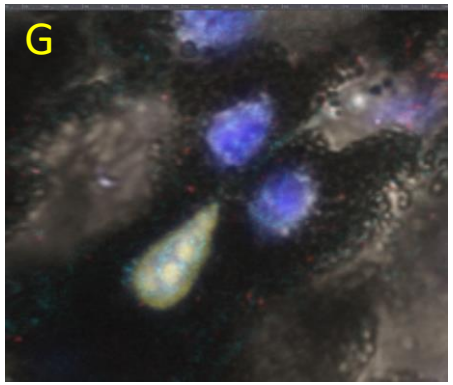

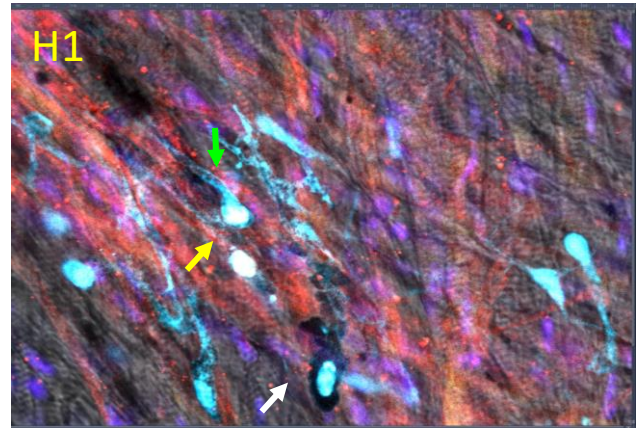

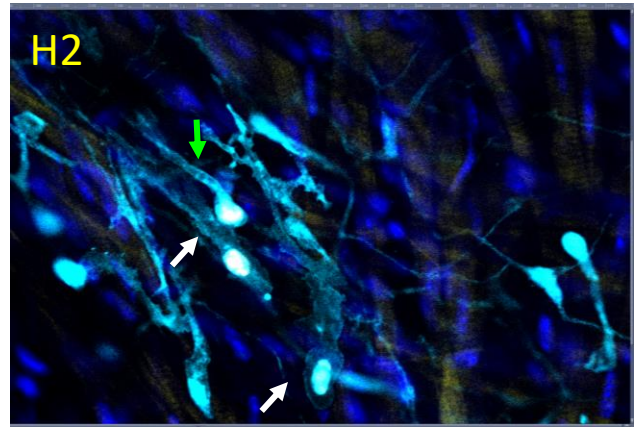

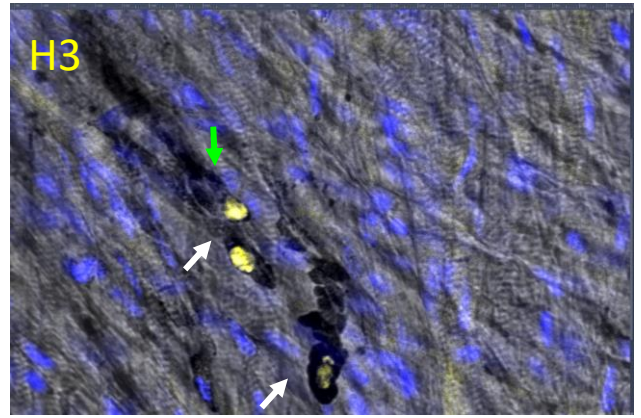

Fig.13

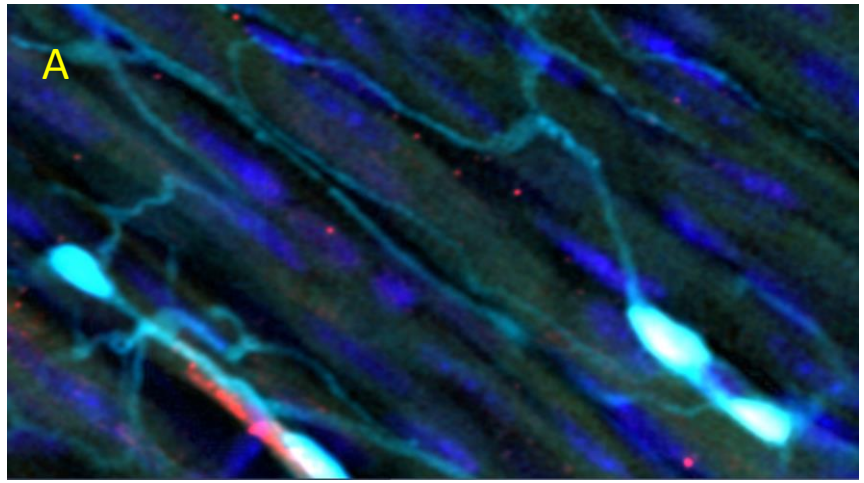

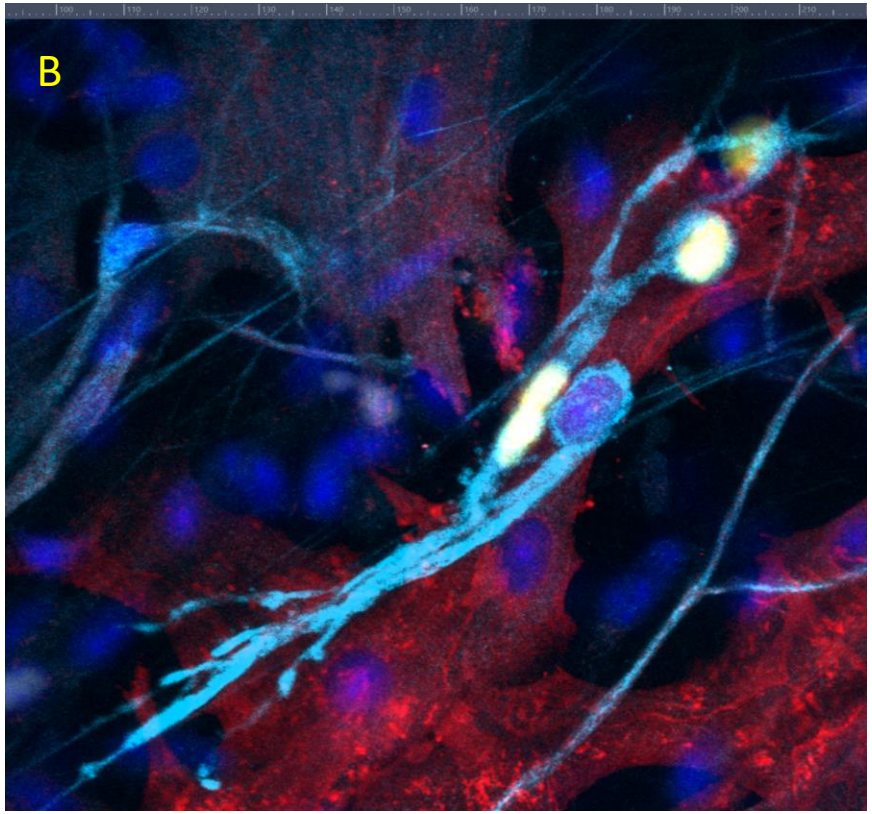

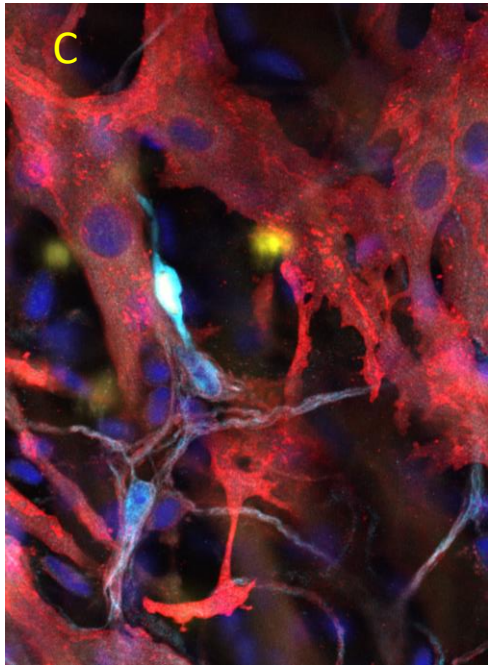

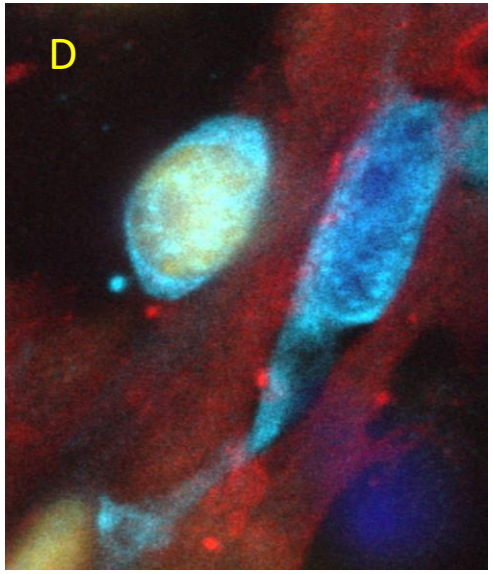

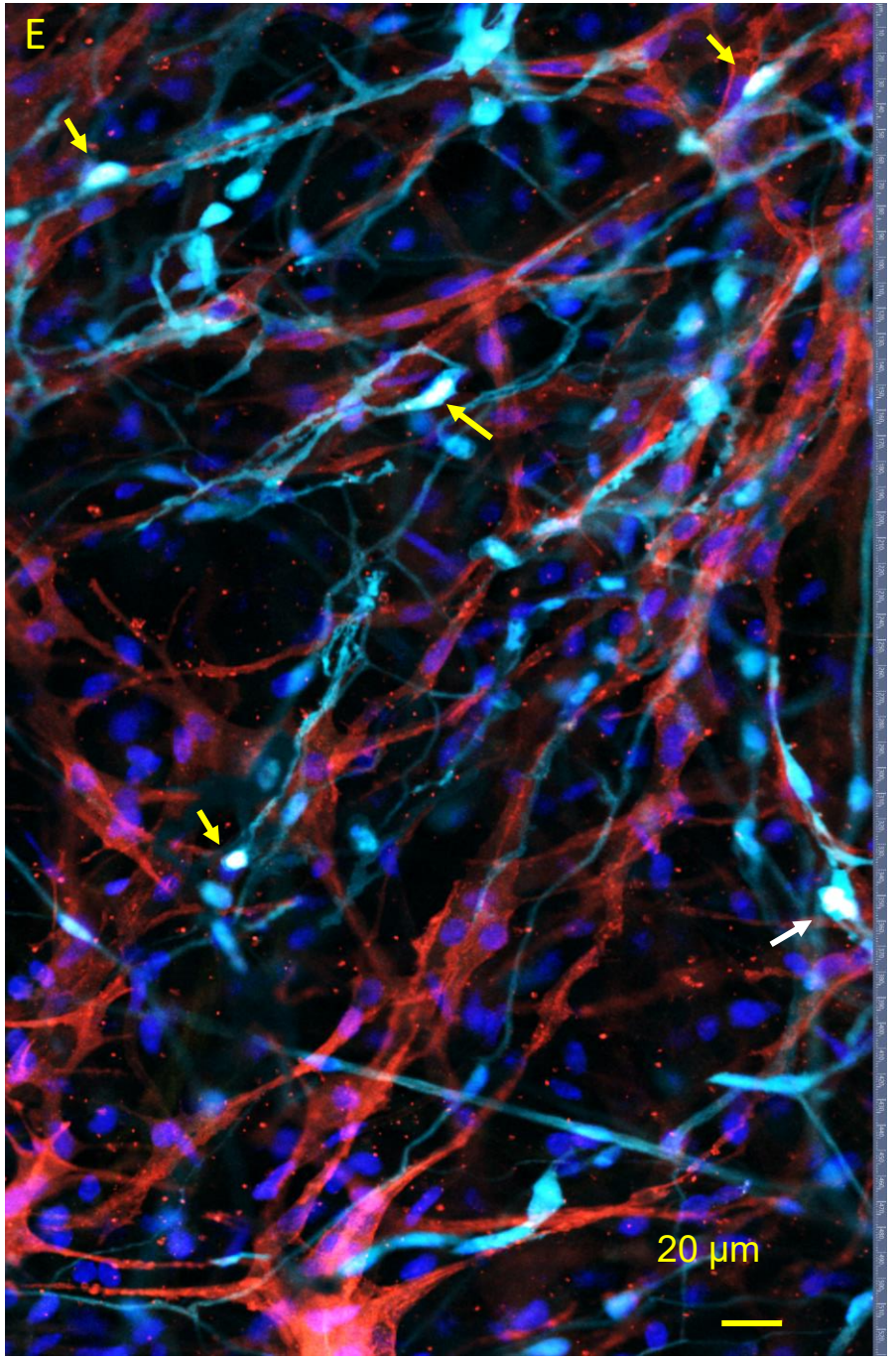

Fig.14

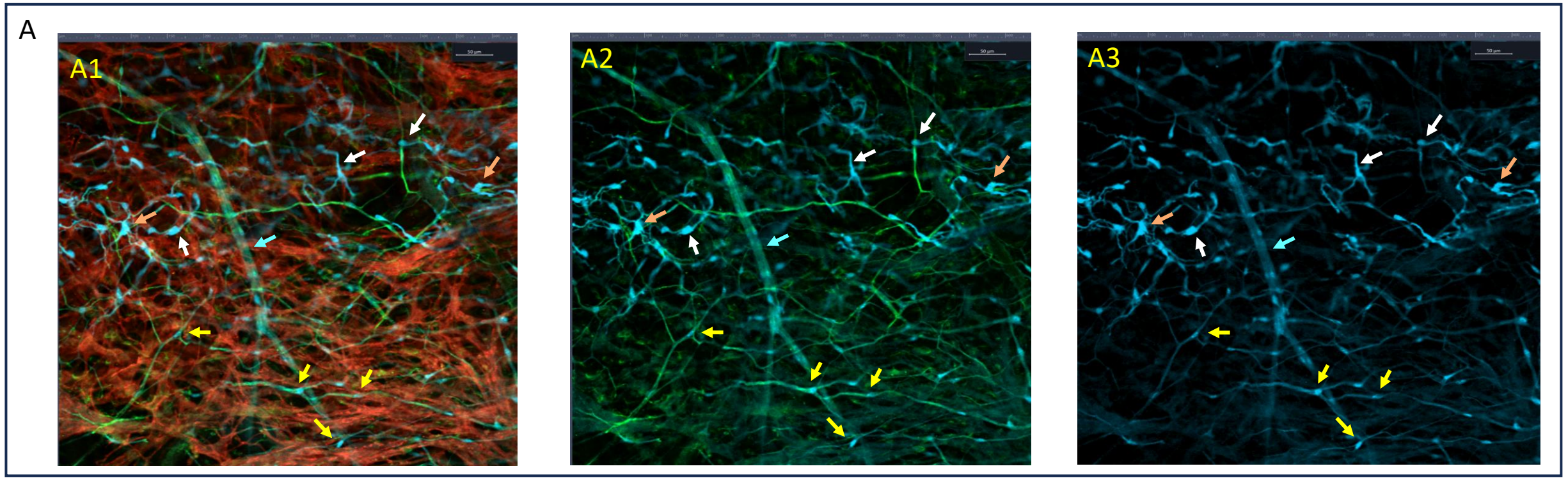

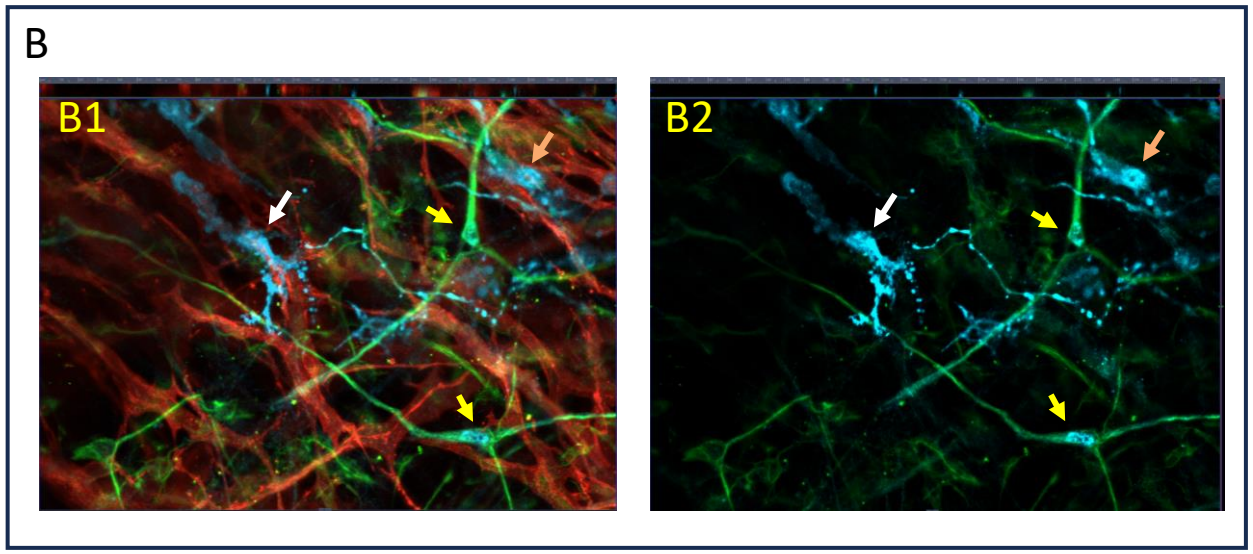

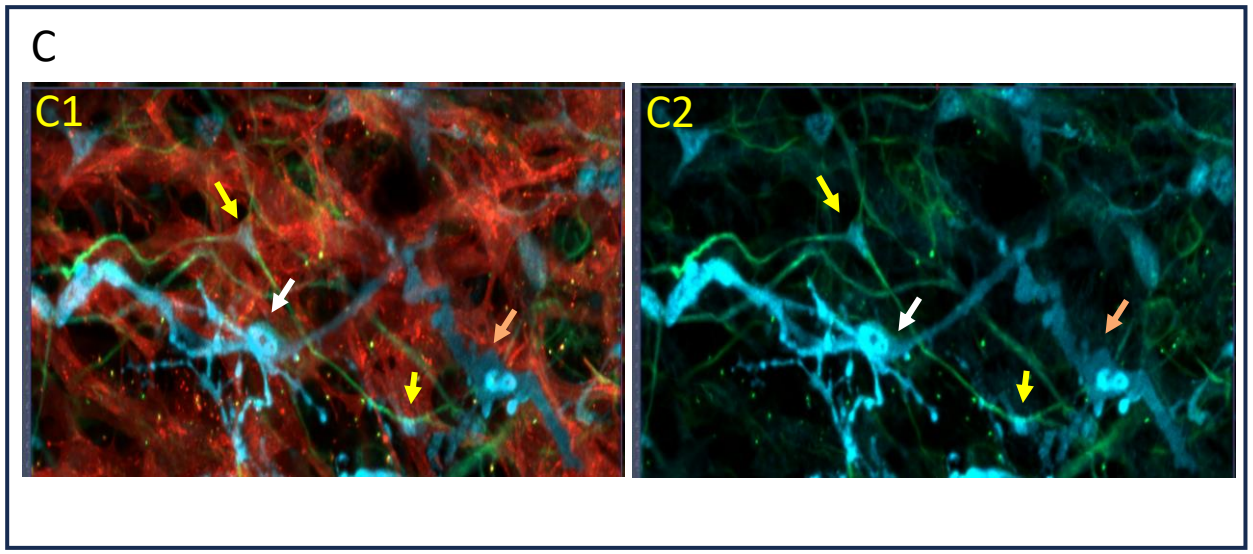

Fig. 1 supplement

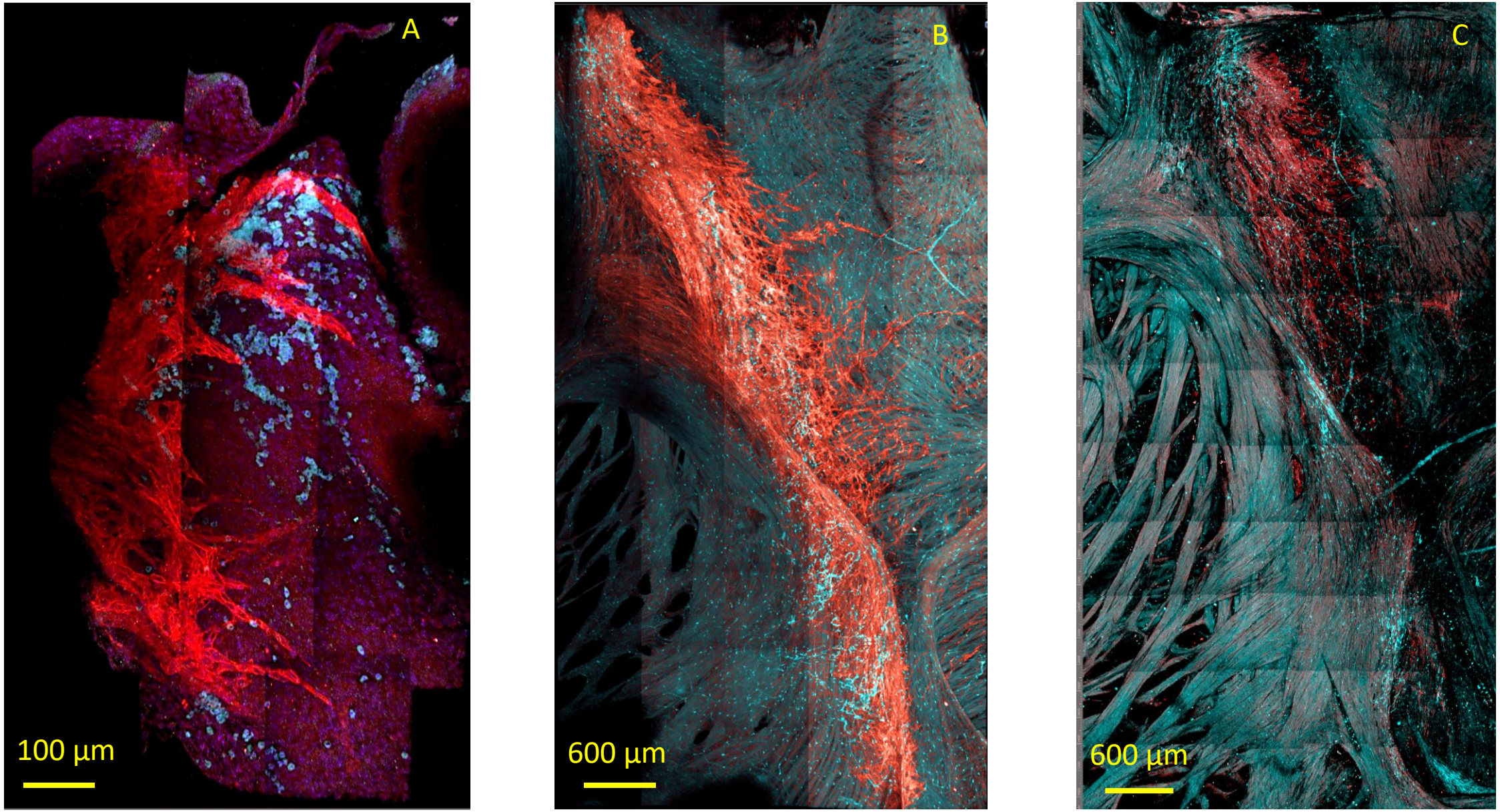

Fig. 2 supplement